

Accepted Manuscript

A hybrid camera- and ultrasound-based approach for needle localization and tracking using a 3D motorized curvilinear ultrasound probe

Mohammad I. Daoud, Abdel-Latif Alshalalfah, Otmane Ait Mohamed, Rami Alazrai

PII: S1361-8415(18)30763-1
DOI: <https://doi.org/10.1016/j.media.2018.09.006>
Reference: MEDIMA 1411



To appear in: *Medical Image Analysis*

Received date: 4 January 2018
Revised date: 11 August 2018
Accepted date: 25 September 2018

Please cite this article as: Mohammad I. Daoud, Abdel-Latif Alshalalfah, Otmane Ait Mohamed, Rami Alazrai, A hybrid camera- and ultrasound-based approach for needle localization and tracking using a 3D motorized curvilinear ultrasound probe, *Medical Image Analysis* (2018), doi: <https://doi.org/10.1016/j.media.2018.09.006>

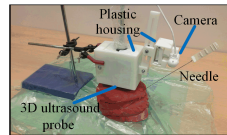
This is a PDF file of an unedited manuscript that has been accepted for publication. As a service to our customers we are providing this early version of the manuscript. The manuscript will undergo copyediting, typesetting, and review of the resulting proof before it is published in its final form. Please note that during the production process errors may be discovered which could affect the content, and all legal disclaimers that apply to the journal pertain.

Highlights

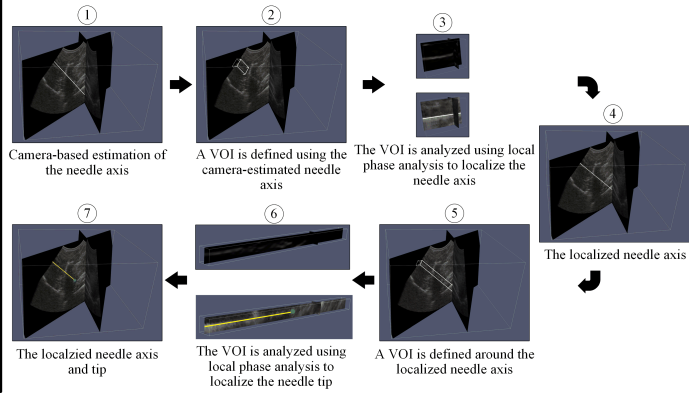
- A new method is developed to localize and track the needle in ultrasound volumes acquired by 3D motorized curvilinear ultrasound probes
- An initial estimation of the needle axis is obtained using a low-cost camera mounted on the ultrasound probe
- Ultrasound-based local phase analyses are employed to refine the initially-estimated needle axis and accurately localize the need tip
- Dynamic needle tracking in a sequence of 3D ultrasound volumes is achieved using a tracking loop that employs a Kalman filter
- The performance results obtained based on *ex vivo* animal experiments suggest the feasibility of applying the proposed method to localize and track the needle using 3D motorized curvilinear ultrasound probes

Graphical Abstract

Experimental Imaging Setup



Needle Detection Procedure



ACCEPTED MANUSCRIPT

A hybrid camera- and ultrasound-based approach for needle localization and tracking using a 3D motorized curvilinear ultrasound probe

Mohammad I. Daoud^{a,*}, Abdel-Latif Alshalalfah^a, Otmane Ait Mohamed^b, Rami Alazrai^a

^aDepartment of Computer Engineering, German Jordanian University, Amman, Jordan

^bDepartment of Electrical and Computer Engineering, Concordia University, Montreal, Quebec, Canada

Abstract

Three-dimensional (3D) motorized curvilinear ultrasound probes provide an effective, low-cost tool to guide needle interventions, but localizing and tracking the needle in 3D ultrasound volumes is often challenging. In this study, a new method is introduced to localize and track the needle using 3D motorized curvilinear ultrasound probes. In particular, a low-cost camera mounted on the probe is employed to estimate the needle axis. The camera-estimated axis is used to identify a volume of interest (VOI) in the ultrasound volume that enables high needle visibility. This VOI is analyzed using local phase analysis and the random sample consensus algorithm to refine the camera-estimated needle axis. The needle tip is determined by searching the localized needle axis using a probabilistic approach. Dynamic needle tracking in a sequence of 3D ultrasound volumes is enabled by iteratively applying a Kalman filter to estimate the VOI that includes the needle in the successive ultrasound volume and limiting the localization analysis to this VOI. A series of *ex vivo* animal experiments are conducted to evaluate the accuracy of needle localization and tracking. The results show that the proposed method can localize the needle in individual ultrasound volumes with maximum error rates of 0.7 mm for the needle axis, 1.7° for the needle angle, and 1.2 mm for the needle tip. Moreover, the proposed method can track the needle in a sequence of ultrasound volumes with maximum error rates of 1.0 mm for the needle axis, 2.0° for the needle angle, and 1.7 mm for the needle tip. These results suggest the feasibility of applying the proposed method to localize and track the needle using 3D motorized curvilinear ultrasound probes.

Keywords: Ultrasound-guided needle interventions, 3D ultrasound imaging, needle localization and tracking, Kalman filter, RANSAC, camera-based needle localization

1. Introduction

Several diagnostic and therapeutic clinical procedures, such as biopsy, therapeutic injection, nerve block, and anesthesia, involve needle interventions. These procedures require accurate needle localization and tracking to improve the success rate of the intervention and reduce the incidence of undesired complications. Ultrasound imaging, which provides a low-cost, real-time, and noninvasive imaging modality, is widely used to

*Corresponding author

Email address: mohammad.aldaoud@gju.edu.jo (Mohammad I. Daoud)

guide needle insertion interventions (Holm & Skjoldbye, 1996; Wisniewski et al., 2010). However, visualizing the needle using conventional two-dimensional (2D) ultrasound with respect to the target anatomy is often challenging due to the need to perfectly align the ultrasound probe to include the needle in the imaging plane. Moreover, the use of 2D ultrasound requires accurate interpretation of the 3D anatomical structures of the patient based on a sequence of 2D ultrasound images, which usually depends on the experience level of the physician. An alternative approach is to use 3D ultrasound to guide needle insertion (Gebhard et al., 2015). In fact, 3D ultrasound, which provides volumetric imaging data, can visualize both the needle and the 3D anatomical structures without the need to perfectly align the ultrasound probe. However, the visibility of the needle in 3D ultrasound volumes might be degraded by several factors, including ultrasound speckle that reduces the quality of ultrasound data, the bright linear structures in the ultrasound volume that have appearance close to the needle, and the reflection of the ultrasound beam by the needle in a direction away from the ultrasound probe (Mwikirize et al., 2017). To address these limitations, automatic needle localization and tracking methods have been developed to detect the needle in 3D ultrasound volumes.

The automatic needle localization and tracking methods can be generally grouped into two classes: methods based on hardware and methods based on software. The hardware-based methods employ complementary devices that enhance the capability to localize and track the needle in 3D ultrasound volumes. For example, Fronheiser et al. (2008) used a piezoelectric actuator to vibrate the needle and employed 3D color Doppler ultrasound imaging to detect the vibrations induced in the needle and the surrounding tissue. A similar approach was proposed in (Adebar & Okamura, 2013) to segment vibrating curved needles using 3D power Doppler ultrasound. Mung et al. (2011) introduced a robust method to track surgical tools using 3D ultrasound. In this method, small ultrasound sensors are placed on the surgical tool to detect the acoustic waves transmitted during 3D ultrasound imaging. The signals received by the sensors are analyzed to compute the 3D position of the surgical tool. Beigi et al. (2015) proposed a method for localizing the needle in 3D ultrasound volumes by moving the needle stylus and detecting the induced intensity variations in the ultrasound volume. The task of localizing the needle was achieved by projecting the volume into two 2D orthogonal image planes and estimating the needle trajectory and tip using these image planes.

One important hardware-based approach for localizing and tracking the needle is to mount cameras on the ultrasound probe to compute the needle position. Computer vision analyses are used to compute the 3D location of the needle with respect to the ultrasound probe based on the camera-visible segment of the needle that is located above the skin. Compared with fixed and wall-mounted cameras, attaching the cameras to the ultrasound probe improves the capability of achieving direct line-of-sight between the cameras and the needle without obstacles (Chan et al., 2005; Khosravi et al., 2007; Najafi et al., 2015; Najafi & Rohling, 2011). The camera-based approach was employed by Chan et al. (2005), in which two stereo cameras mounted on a 2D ultrasound probe were used to estimate the needle trajectory with respect to the cameras. Spatial calibration was carried out to map the estimated needle trajectory to the coordinate system of the 2D ultrasound probe. In fact, this method was separately applied using two high-performance cameras and two

low-cost USB cameras, where the former setup achieved a needle localization accuracy of 3.1 ± 1.8 mm and the latter obtained an accuracy of 6.5 ± 5.7 mm. Khosravi et al. (2007) proposed the use of two cameras to estimate the needle trajectory without the need for spatial calibration. In particular, a training algorithm was applied to compute the mapping between the location of the needle in the 2D camera images and the corresponding needle location in the 3D space. The method enabled 3D needle trajectory estimation with average distance and orientation errors of 2.4 mm and 2.6° , respectively. The camera-based needle localization approach has been employed by a commercial needle tracking system developed by Clear Guide Medical Inc. (Baltimore, MD, United States) that computes the needle position using two stereo cameras mounted on a 2D ultrasound probe. This commercial, camera-based needle tracking system demonstrates the feasibility of using cameras mounted on the ultrasound probe to improve the capability of guiding needle insertion in real-life clinical applications. Najafi et al. (2015) proposed the use of one high-performance camera mounted on a 2D ultrasound probe to estimate the needle trajectory by analyzing the regular marking points that exist in many medical needles, such as biopsy and epidural needles. This method was applied to localize needles inserted in a water bath and scanned using out-of-plane 2D ultrasound imaging with an accuracy of 0.94 ± 0.46 mm. In fact, the use of one camera, instead of two cameras, to estimate the needle position has the advantage of reducing the cost, size, and complexity of the needle localization system. It is worth noting that the one-camera approach has not been demonstrated for 3D ultrasound probes and its performance was not evaluated when a low-cost camera is employed to localize the needle.

The software-based methods localize and track the needle using ultrasound data analysis. In fact, most software-based methods analyze the ultrasound volume to detect features that correspond to the needle structure. For example, principle component analysis (PCA) has been used to detect the needle in 3D ultrasound volumes (Novotny et al., 2003). Barva et al. (2004) proposed the use of the Radon transform to localize the needle based on radio-frequency (RF) signals acquired by a 3D ultrasound probe. Novotny et al. (2007) developed a real-time algorithm to track straight surgical instruments in 3D ultrasound volumes. The algorithm employed the generalized Radon transform to localize the instrument axis and used passive markers placed on the shaft to identify the instrument tip. Mari & Cachard (2007) proposed a method to localize a thin needle inserted in a tissue-mimicking phantom using 3D ultrasound RF data by maximizing the parallel integral projection (PIP) transform, which represents a special form of the Radon transform. An improved needle localization method was introduced in (Barva et al., 2008), in which the needle was detected by computing the PIP transform of the 3D ultrasound volume. The performance of the method was evaluated by localizing the needle in 3D ultrasound volumes acquired for tissue-mimicking phantoms and *in vivo* breast biopsy. Ding et al. (2003) introduced an algorithm to segment the needle in 3D ultrasound volumes by extracting two orthogonal 2D image projections from the 3D volume and analyzing the 2D projections to localize the needle. The method involved cropping the 3D ultrasound volume based on a priori estimate about the needle location and orientation to eliminate the irrelevant complex structures from the 2D projections. Zhou et al. (2007) employed a 3D randomized Hough transform (RHT) for localizing the needle in 3D

ultrasound volumes. The 3D RHT reduced the computational complexity of the classical Hough transform by randomly sampling pairs of voxels in the 3D ultrasound volume after applying thresholding. A faster
80 version of the 3D RHT, called the 3D quick RHT, was introduced in (Qiu et al., 2008), in which a two-stage, coarse-fine search approach was applied to reduce the computational complexity. In (Neshat & Pateluchi, 2008), the localization of curved needles in ultrasound volumes has been achieved by representing the needle using Bézier polynomials and applying a parallel implementation of the generalized Radon transform.

Another important software-based approach for localizing the needle is to use the random sample consen-
85 sus (RANSAC) algorithm (Fischler & Bolles, 1981). This approach was used by Uherčík et al. (2010) who used a model-fitting RANSAC (MF-RANSAC) algorithm to localize the needle in 3D ultrasound volumes. The MF-RANSAC algorithm enabled accurate needle localization in simulated ultrasound volumes and experimental ultrasound volumes of high quality. However, the accuracy and robustness of needle localization were reduced when the MF-RANSAC algorithm was applied for realistic ultrasound volumes with complex
90 background. Zhao et al. (2013) proposed a two-phase needle tracking method, called region of interest (ROI) combined with the RANSAC and Kalman filter (ROI-RK), to overcome the limitations of the MF-RANSAC algorithm and support dynamic needle tracking in a sequence of 3D ultrasound volumes. In the first phase, the ROI-RK method processes the first ultrasound volume using a 3D line filter and the MF-RANSAC algorithm to estimate the needle. Moreover, the estimated needle is used to define a VOI around it. In the
95 second phase, the location of the VOI that includes the needle is estimated in the next ultrasound volume of the 3D sequence by employing a speckle tracking algorithm to compute the velocity of the needle tip and the Kalman filter to update the position of the VOI. The updated VOI is processed using the MF-RANSAC algorithm to estimate the needle in the next ultrasound volume. Moreover, the Kalman filter is employed to refine the estimated location of the needle. This tracking loop is iteratively applied until the needle is
100 tracked in all volumes of the 3D ultrasound sequence. In a recent study (Zhao et al., 2017), the performance of the ROI-RK method was compared with three other needle localization and tracking methods that are based on PCA, RHT, and PIP. The performance evaluations quantified the capability of the four methods to estimate the needle in both the static and dynamic situations in simulated and experimental ultrasound volumes. The results indicated that the ROI-RK method outperformed the three other methods based on
105 combined metrics of needle localization and tracking accuracies and execution times.

In the majority of software-based methods, the needle is assumed to appear in the 3D ultrasound volume as a linear structure with intensity higher than the background. However, this assumption might not be satisfied in some real-life clinical scenarios. For example, in curvilinear ultrasound images and volumes, the needle is mainly visible at the needle segment in which the ultrasound beam is perpendicular to the
110 needle (Hacihaliloglu et al., 2015; Daoud et al., 2015). Moreover, the ultrasound volume might include other needle-like structures that can mislead the software-based methods. Some software-based methods, such as the PIP- and RANSAC-based methods, can be affected by the gain settings of the ultrasound machine. For instance, if the gain is increased to improve the contrast, the noise signals can be magnified and the

ultrasound volume can be affected by ultrasound artifacts and speckle that degrade the needle localization
115 accuracy.

One effective technique to achieve intensity-invariant ultrasound-based analysis is to use the local phase. In fact, Oppenheim & Lim (1981) showed that the contribution of the phase information of a particular image to its visual appearance outweighs the magnitude information. Intensity-invariant local-phase methods have been proposed in the literature to extract the bone surface in 2D (Hacihaliloglu et al., 2009) and 3D
120 (Hacihaliloglu et al., 2012) ultrasound data and classify breast ultrasound images (Cai et al., 2015). Moreover, Beigi et al. (2017) and Hacihaliloglu et al. (2015) employed local phase analysis to localize the needle in 2D ultrasound images. Mwikirize et al. (2017) proposed the use of 2D local phase analysis to detect the needle in linear 3D ultrasound volumes. In particular, a local phase descriptor is applied to each 2D slice in the 3D ultrasound volume to quantify the straight linear structures that are similar to the needle. After applying
125 the local phase descriptor, each slice is processed using a needle detector, which is based on normalized histograms of oriented gradients descriptors and a linear support vector machine classifier, to identify the slices that include the needle and combine these slices into one sub-volume. In the second stage, the sub-volume is processed to enhance the visibility of the needle and localize the needle tip. The results reported in (Mwikirize et al., 2017) showed that the method can obtain good results for needles inserted in *ex vivo*
130 bovine tissue that are scanned using a 3D motorized linear ultrasound probe. One potential limitation of this method is the fact that real-life, clinical 3D ultrasound volumes can include other strong, needle-like, linear structures, which might mislead the process of identifying the 2D slices that correspond to the needle. Pourtaherian et al. (2017) proposed a method to detect the best view to visualize medical instruments, including needles, in 3D ultrasound volumes. The method is composed of three stages. In the first stage, the
135 ultrasound volume is preprocessed to enhance the appearance of the medical instrument and reduce noise. In the second stage, the voxels of the ultrasound volume are classified using linear support vector machine and linear discriminant analysis classifiers to identify the voxels that belong to the medical instrument. The classification is performed using descriptors that are based on the raw values of the voxels, the outcome of vesselness filtering, and the outcome of Gabor transformation. In the third stage, the axis of the instrument
140 is estimated by fitting a mathematical model that describes the instrument to the classified voxels. The performance of the method has been evaluated using *in vitro*, *ex vivo*, and *in vivo* datasets. One limitation of this method is that it does not support the detection of the needle tip. Moreover, the long processing time of the method, which is between 2 and 4 minutes, might limit its use in real-life clinical applications.

A large group of commercial 3D ultrasound imaging systems employs motorized curvilinear probes
145 (Pospisil et al., 2010; Gao et al., 2016). Hence, 3D motorized curvilinear probes [provide an attractive means](#) to enable 3D ultrasound guidance of needle insertion interventions. Generally, curvilinear ultrasound probes achieve better needle visibility at clinically-relevant needle insertion angles compared with linear transducers. This can be attributed to the high probability of obtaining perpendicular interception between the needle and the ultrasound beams of curvilinear probes (Tsui et al., 2009). However, the spacing between

150 the ultrasound beams transmitted by 3D motorized curvilinear probes increases as a function of depth, which might degrade the visibility of the needle. Therefore, the development of automatic, accurate, reliable, and efficient needle localization and tracking methods contributes to the ongoing efforts to improve the use of 3D motorized curvilinear ultrasound probes, which provide extended 3D field-of-view compared to 2D ultrasound probes, to enhance the outcome and safety of needle insertion interventions. The automatic and accurate
 155 localization of the needle enables the physician to concentrate on manipulating the 3D ultrasound probe to visualize the target anatomy and enhancing the alignment between the needle and the target. Moreover, the automatic and accurate localization of the needle reduces the risk of affecting important anatomical structures in the body, such as vessels and nerves, and hence improves the safety of the intervention.

In the current study, we propose a hybrid method that combines both hardware- and software-based
 160 analyses to enable accurate and robust needle localization and tracking using 3D motorized curvilinear ultrasound probes. The method employs a single low-cost camera mounted on the ultrasound probe to obtain an approximate estimation of the needle axis. In fact, the algorithm proposed in (Najafi et al., 2015) to localize the needle in 2D ultrasound images using a single high-performance camera has been employed in the current study to approximately estimate the needle axis using a low-cost camera. The camera-estimated
 165 needle axis and the imaging geometry of the 3D motorized curvilinear probe are analyzed to identify a VOI in the ultrasound volume, called VOI_{Axis} , that enables high needle visibility. VOI_{Axis} is processed using local phase analysis and the MF-RANSAC algorithm to achieve accurate localization of the needle axis. The location of the needle tip along the axis is determined using a probabilistic approach that quantifies the characteristics of the local phase within a VOI, called VOI_{Tip} , that surrounds the needle axis. Needle
 170 tracking is enabled by employing a tracking loop to estimate the VOIs in the consecutive ultrasound volumes that include the needle and limiting the needle estimation analysis to these VOIs.

The main objective of our study is to provide an innovative approach to utilize the initial estimation of the needle axis, which is obtained using the low-cost camera, to enable reliable, accurate, and efficient ultrasound-based localization and tracking of the needle in ultrasound volumes acquired by 3D motorized
 175 curvilinear ultrasound probes. Specifically, the main contributions of the current study can be summarized as follows:

- For curvilinear ultrasound probes, the visibility of the needle is maximal when the transmitted ultrasound beams intercept perpendicularly or near perpendicularly with the needle (Daoud et al., 2011, 2015; Hacıhaliloglu et al., 2015). In our study, we have analyzed the camera-based estimation of the
 180 needle axis and the imaging geometry of the 3D motorized curvilinear ultrasound probe to identify VOI_{Axis} that enables high needle visibility. The main characteristic of VOI_{Axis} is that the ultrasound beams transmitted by the ultrasound probe intercept perpendicularly or near perpendicularly with the needle. Hence, accurate, reliable, and efficient localization of the needle axis can be achieved by limiting the ultrasound-based analysis for localizing the needle axis to VOI_{Axis} . It is worth noting that
 185 localizing the needle axis by analyzing the entire ultrasound volume might increase the failure rate and

degrade the localization accuracy due to the presence of other needle-like structures in the ultrasound volume that can lead to incorrect localization of the needle axis. Moreover, limiting the localization analysis of the needle axis to VOI_{Axis} reduces the computational complexity of our proposed method.

- 190 • The procedure employed to analyze VOI_{Axis} aims to ensure accurate and efficient localization of the needle axis. In particular, VOI_{Axis} is oriented such that the majority of the ultrasound beams that are perpendicular or nearly-perpendicular to the needle passes through its top face. Hence, our proposed method aims to detect the strong needle reflections of the ultrasound beams that take place within VOI_{Axis} by applying 2D phase congruency analysis (Kovesi, 2003, 1999) to the 2D image planes in VOI_{Axis} that are parallel to its front face. Moreover, the capability of detecting the orthogonal needle reflections of the ultrasound beams is optimized by applying the 2D phase congruency analysis along

195 the direction orthogonal to the top face of VOI_{Axis} . Hence, our approach enables intensity-invariant, orientation-specific detection of the strong needle reflection that take place within VOI_{Axis} using the low complexity 2D phase congruency analysis, instead of using the computationally-intensive 3D phase congruency analysis.
- 200 • Accurate and efficient localization of the needle tip is achieved by defining VOI_{Tip} around the accurately localized needle axis. VOI_{Tip} is analyzed using the intensity-invariant, orientation-specific, low-complexity 2D phase congruency analysis, which is described in the previous point, to detect the edges that correspond to the needle. Moreover, a new probabilistic approach is used to analyze the detected needle-specific edges with the goal of achieving accurate localization of the needle tip.
- 205 • Needle tracking is enabled by employing a tracking loop to estimate the VOIs in the consecutive ultrasound volumes that include the needle and limiting the needle estimation analysis to these VOIs. This tracking loop limits the requirement of having direct line-of-sight between the camera and the needle to the first ultrasound volume as well as the incidents of needle tracking re-initialization in the consecutive ultrasound volumes.
- 210 • The performance of our proposed method is evaluated by localizing and tracking needles inserted in different *ex vivo* animal specimens that have various ultrasound echogenicity characteristics. Moreover, we have compared the performance our proposed method with a well-studied method that was introduced by Zhao et al. (2013). The experimental results reported in the current study demonstrate the feasibility of applying our proposed method to enable reliable, accurate, and efficient localization

215 and tracking of the needle using 3D motorized curvilinear ultrasound probes.

The remainder of the paper is organized as follows. Section 2 presents the proposed needle localization and tracking method. The experiments and analyses employed to evaluate the performance of the proposed method are provided in section 3. The results, discussion, and conclusion are presented in sections 4, 5, and 6, respectively.

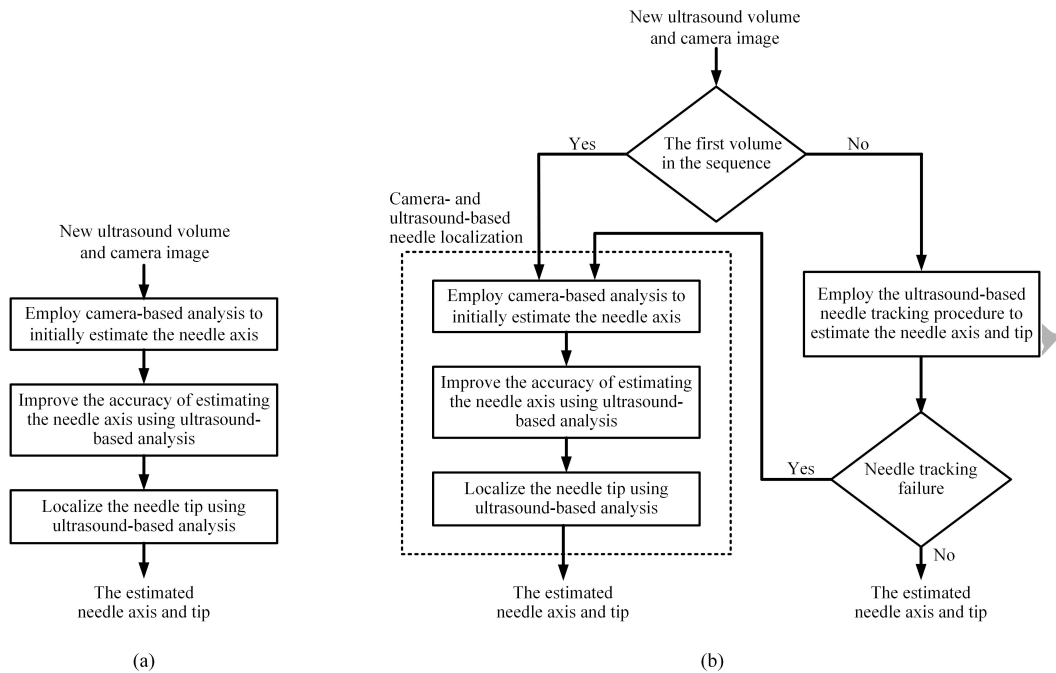


Figure 1: (a) A block diagram that summarizes the needle localization in the static situation. (b) A block diagram that summarizes the needle tracking in the dynamic situation.

2. Methods

The method proposed to localize and track the needle using 3D motorized curvilinear ultrasound probes is composed of four components. The first three components are focused on needle localization, as illustrated in Fig. 1(a). In particular, these components include the use of a low-cost camera to approximately estimate the needle axis in the ultrasound volume, improve the localization accuracy of the needle axis by employing ultrasound-based analysis, and identify the location of the needle tip by analyzing the ultrasound voxels surrounding the needle axis. The last component is focused on customizing the first three parts to enable accurate needle tracking, as shown in Fig. 1(b).

2.1. Imaging apparatus

3D ultrasound imaging was carried out using a SonixTOUCH Q+ ultrasound system (BK Ultrasound, Herlev, Denmark). The system was equipped with a 3D motorized curvilinear ultrasound probe (Model 4DC7-3/40, BK Ultrasound) that has a center frequency of 5 MHz and -6 -dB bandwidth of 3 MHz. This probe enables the acquisition of 3D ultrasound volumes by mechanically sweeping a 2D curvilinear ultrasound transducer back and forth around a fixed rotation axis. Detailed description of the imaging geometry employed in the 4DC7-3/40 probe is provided in subsection 2.3.1.

A low-cost USB web camera (IceCam2, Macally Peripherals, Ontario, CA, United States) was attached to the 3D ultrasound probe using a plastic housing, as shown in Fig. 2(a). This web camera offers the advantages of lightweight and compact size. The camera acquires images with a resolution of 640×480

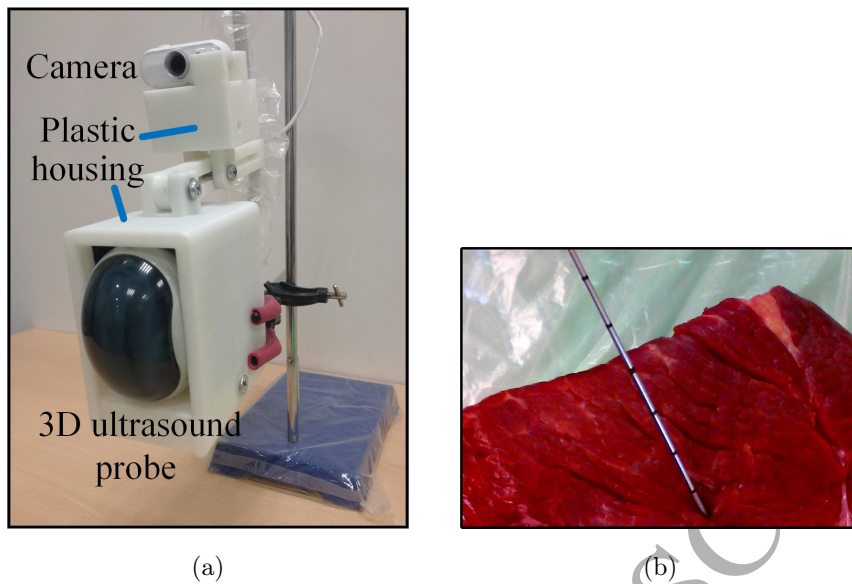


Figure 2: (a) The imaging apparatus that includes the 3D ultrasound probe, the USB web camera, and the plastic housing. (b) A camera image acquired for a needle inserted in a bovine muscle specimen.

pixels at a maximum frame rate of 30 frames per second and can focus to distances as small as 20 mm. In the current study, the focus of the camera was adjusted and fixed to obtain clear images of the needle, which is located between 40 to 80 mm away from the camera. The plastic housing was designed using a computer-aided design (CAD) software and manufactured using 3D printing technology to rigidly fix the camera to the 3D ultrasound probe. Therefore, the spatial transformation between the camera and the ultrasound probe remained constant throughout the experiments.

2.2. The camera-based estimation of the needle axis

Najafi et al. (2015) proposed an analytical method for localizing the needle in 2D ultrasound images using a single high-performance camera mounted on the ultrasound probe. This method is employed in the current study to approximately estimate the position of the needle axis in the 3D ultrasound volume using a low-cost camera.

The camera-based method starts by calibrating the camera using a standard calibration algorithm (Heikkila & Silven, 1997) to determine its intrinsic parameters, including the focal length (f_x, f_y) and the principle point (g_x, g_y) . This calibration process is carried out for one time. The 3D position of the linear needle axis is estimated by identifying a set of N marking points, $\{Q_1, Q_2, \dots, Q_N\}$, in the camera 2D image that are collinearly located along the needle and mapping these points into their corresponding locations, $\{P_1, P_2, \dots, P_N\}$, in the world 3D coordinate system. In fact, the uniformly-spaced edge markings that exist in many medical needles are used as marking points to localize the needle. Accurate identification of the needle marking points, $\{Q_1, Q_2, \dots, Q_N\}$, in the camera image is achieved using an automated algorithm that is developed by Najafi et al. (2015). Moreover, Najafi et al. (2015) proposed a closed-form solution

to map the camera-image needle marking points, $\{Q_1, Q_2, \dots, Q_N\}$, into the matching 3D world points, $\{P_1, P_2, \dots, P_N\}$, based on the linear structure of the needle and the known regular spacing between any consecutive needle marking points. This closed-form solution requires a minimum of three marking points to estimate the 3D location of the needle axis. It is worth noting that the results reported in (Najafi et al., 2015) indicate that accurate tracking of the needle axis can be achieved using 5 to 7 needle marking points. Hence, in all needle experiments performed in the current study, the plastic housing that holds the camera and the 3D ultrasound probe was oriented such that a minimum of five needle marking points are included in the camera images. Figure 2(b) shows an example camera image acquired for a needle inserted in a bovine muscle specimen, where the visible part of the needle includes six needle marking points.

After identifying the needle marking points, $\{Q_1, Q_2, \dots, Q_N\}$, and mapping them to the corresponding world 3D points, $\{P_1, P_2, \dots, P_N\}$, the 3D position of the needle axis is estimated with respect to the camera. Hence, spatial calibration is required to transform the 3D needle position from the camera coordinate system to the ultrasound coordinate system. In the current study, the camera-to-ultrasound calibration is performed using the single-wall method (Prager et al., 1998).

2.3. Refining the camera-based estimation of the needle axis using ultrasound-based analysis

The 3D pose of the needle axis obtained using the low-cost camera is expected to be located within an approximate region around the true needle axis. Hence, accurate estimation of the needle axis can be achieved by defining a VOI, called VOI_{Axis} , around the camera-estimated needle axis and employing ultrasound-based analysis to localize the needle axis within VOI_{Axis} . To enable effective ultrasound-based analysis, it is important to consider the imaging geometry of the 3D motorized ultrasound probe and analyze the interaction between the ultrasound beams transmitted during 3D ultrasound imaging and the needle. Hence, in the following, we will describe the imaging geometry of 3D motorized curvilinear ultrasound probes, with special focus on the 4DC7-3 probe employed in the current study. This understanding of the imaging geometry will enable the identification of VOI_{Axis} that enables high needle visibility. The identified VOI_{Axis} is processed to extract a local phase feature map that provides an intensity-invariant measure to detect the needle axis. This feature map is processed using the MF-RANSAC algorithm (Uherčík et al., 2010) to accurately localize the needle axis.

2.3.1. The imaging geometry of 3D motorized curvilinear ultrasound probes

In 3D motorized curvilinear probes, including the 4DC7-3 probe employed in the current study, ultrasound imaging is performed by mechanically sweeping a 2D curvilinear ultrasound transducer back and forth around a fixed rotation axis that is parallel to the aperture of the transducer, as illustrated in Fig. 3(a). The rotation radius, a , is defined as the spacing between the rotation pivot point and the center of aperture of the 2D transducer, as shown in Fig. 3(b). To acquire a 3D ultrasound volume, the 2D transducer is rotated along the sweep (elevation) direction, ϕ , to collect a set of 2D curvilinear image frames that covers an elevation field of view (FOV), denoted by Φ . The acquired ultrasound image frames, which form a fan shape, are

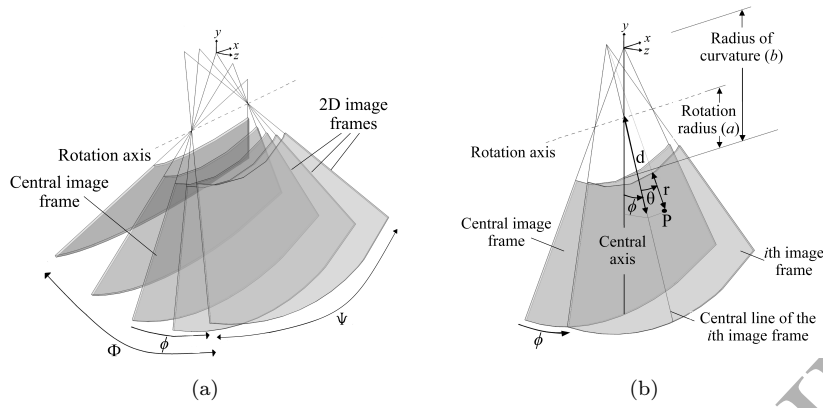


Figure 3: (a) The imaging geometry employed by a 3D motorized curvilinear ultrasound probe, in which a 2D curvilinear transducer is rotated along the elevation direction, ϕ , to acquire 2D image frames that cover an elevation FOV, Φ . Each image frame covers a fixed aperture angle, Ψ . (b) The mapping between the local position of a point, p , located at the i th 2D image frame and the 3D coordinate system, (x, y, z) , of the ultrasound volume can be computed based on the rotation radius, a , the radius of curvature, b , the axial spacing, r , between p and the 2D transducer aperture, the azimuth angle, θ , between p and the central line of the i th image frame, and the elevation angle, ϕ , between the i th image frame and the central image frame.

processed to construct a 3D ultrasound volume. The image frame located at $\phi = 0$, which is called in this study the central image frame, includes the central axis of the 3D probe. The 2D curvilinear transducer has a fixed aperture angle, Ψ , and a fixed radius of curvature, b . For the 4DC7-3 probe used in this study, the values of a , b , Φ , and Ψ are equal to 27.25 mm, 39.8 mm, 75°, and 79°, respectively.

Consider the i th 2D image frame that is acquired at elevation angle ϕ with respect to the central image frame as shown in Fig. 3(b). The location of a point, p , within the i th 2D image frame can be described by the polar 2D coordinate, $(r + b, \theta)$, where r is the axial spacing between p and the aperture of the 2D transducer, b is the radius of curvature of the 2D transducer, and θ is the angle between p and the central line of the i th image frame. The location of p in the 3D Cartesian coordinate system, (x, y, z) , of the ultrasound volume synthesized by the 3D probe can be computed based on the local location of p , $(r + b, \theta)$, within the i th 2D image frame and the elevation angle, ϕ , of the i th image frame as described in (Harris et al., 2007).

2.3.2. Identifying VOI_{Axis} that enables high needle visibility in the 3D ultrasound volume

As described previously, the camera-based estimation of the needle axis and the imaging geometry of motorized curvilinear ultrasound probes, particularly the 4DC7-3/40 probe, can be analyzed to identify a VOI, denoted by VOI_{Axis} , that enables high needle visibility in the 3D ultrasound volume. In fact, our approach to identify VOI_{Axis} is to analyze the interaction between the needle and the ultrasound beams transmitted during the acquisition of the individual 2D image frames that synthesize the 3D ultrasound volume. At the beginning, we will analyze the interaction between the needle and the ultrasound beams transmitted during the acquisition of one of the 2D image frames that compose the ultrasound volume with the goal of identifying a segment of the needle that enables high needle visibility in this 2D image frame. This analysis is extended to enable the identification of a needle segment that enables high needle visibility

in the 3D ultrasound volume. Since the exact location of the needle in the ultrasound volume is unknown, the camera-based estimation of the needle axis is used to obtain an approximate detection of the needle segment that enables high needle visibility in the 3D ultrasound volume. This camera-based estimation of the needle segment with high needle visibility is employed to identify the location and orientation of VOI_{Axis} in the 3D ultrasound volume.

Due to the significant mismatch between the acoustic impedance of the metal needle and that of the surrounding soft tissue, ultrasound reflection at the needle surface generates acoustic echoes with high amplitude (Daoud et al., 2015, 2011). Therefore, the brightness of the needle is expected to be higher than the surrounding tissue. For 2D curvilinear ultrasound transducers, the strongest needle echoes are generated when the ultrasound beam is perpendicular or nearly perpendicular to the needle (Daoud et al., 2011, 2015; Hacihaliloglu et al., 2015). The ultrasound beams that intercept perpendicularly with the needle, and hence generate the strongest needle echoes, are generated by the transducer elements that are located around the line that extends from the center of curvature of the 2D curvilinear transducer and orthogonally intercepts with the needle axis, where this line is called the *orthogonal needle line*. On the other hand, the transducer elements that are located away from the orthogonal needle line along the azimuth angular direction are expected to receive needle echoes with low energy due to the directivity effect of the piezoelectric elements. In fact, the study by Daoud et al. (2015) indicated that for the 2D curvilinear transducer of the 4DC7-3/40 probe, the energy of the needle echoes received by the individual transducer elements drops below 10% of the energy of the strongest echoes received from the needle when the azimuth angular spacing between the transducer elements and the orthogonal needle line exceeds 20° . Hence, the elements of the 2D curvilinear transducer that are expected to enable the highest needle visibility are located within an azimuth interval, Ω , where the length of Ω is affected by the directivity of the piezoelectric elements and its azimuth center is positioned at the orthogonal needle line. For the 2D curvilinear transducer of the 4DC7-3 probe, the length of the azimuth interval Ω is equal to 40° (Daoud et al., 2015). The 2D curvilinear ultrasound image shown in Fig. 4(a) illustrates the azimuth interval, Ω , that is expected to enable high needle visibility. This ultrasound image is acquired by the 2D curvilinear transducer of the 4DC7-3/40 probe for a needle placed in water bath. During ultrasound image acquisition, the 2D curvilinear transducer of the 4DC7-3/40 probe is fixed at an elevation angle, ϕ , of 0° . The insertion angle and axial location of the needle are around 0° and 45 mm, respectively. Moreover, the needle is oriented such that it is included in the imaging plane of the 2D curvilinear transducer. As shown in Fig. 4(a), the highest needle visibility is obtained by the transducer elements that are located within the azimuth interval, Ω , that has a length of 40° . In addition to the azimuth interval, Ω , the needle visibility in a given 2D image frame depends on the portion of the needle that is located within this image frame. Figure 4(b) illustrates the interaction between the ultrasound beams transmitted during the acquisition of the i th 2D image frame, which is located at elevation angle ϕ , and the needle. The needle segment that enables high needle visibility in the 2D ultrasound image frame corresponds to the intersection between the azimuth interval, Ω , and the portion of the needle that is located within this

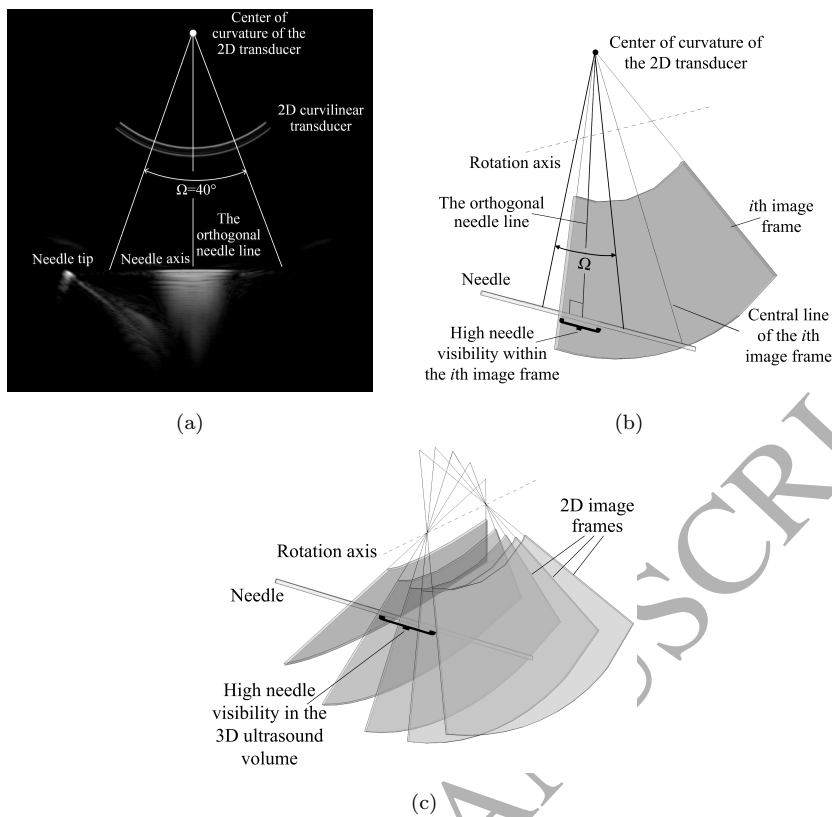


Figure 4: (a) An ultrasound image acquired by the 2D curvilinear transducer of the 4DC7-3/40 probe for a needle inserted in water bath. The 2D curvilinear transducer is fixed at an elevation angle, ϕ , of 0° . The needle is placed such that its insertion angle is 0° and axial location is around 45 mm. The strongest needle echoes are mainly within the azimuth interval, $\Omega = 40^\circ$, where the center of this interval is located at the orthogonal needle line. (b) Schematic illustration of the needle segment that enables high needle visibility within the i th image frame. This needle segment can be identified as the intersection between the azimuth interval, Ω , defined around the orthogonal needle line and the portion of the needle located within the i th image frame. (c) The portion of the needle that achieves high needle visibility within the 3D ultrasound volume corresponds to the ensemble of all high-visibility needle segments computed for the 2D image frames that synthesize the volume.

image frame, as shown in Fig. 4(b). It is worth noting that if the azimuth interval, Ω , is located outside the 2D ultrasound image frame, then the needle segment with high needle visibility cannot be defined for this image frame.

The concept of the needle segment with high needle visibility can be extended into the 3D ultrasound volume by analyzing all 2D image frames that synthesize the volume to identify the needle segments with high visibility within these 2D image frames. The ensemble of these segments defines the portion of the needle that enables high needle visibility within the 3D ultrasound volume. Figure 4(c) provides a schematic representation of a 3D ultrasound volume acquired for a needle and the portion of the needle that enables high needle visibility in the 3D ultrasound volume.

As described previously, since the location of the true needle in the ultrasound volume is unknown, the camera-estimated needle axis, which provides an approximation of the true needle axis, is used to estimate the region in the ultrasound volume that enables high needle visibility. In particular, each of the 2D image

frames that compose the 3D ultrasound volume is analyzed individually to estimate the portion of the camera-estimated needle axis that would enable high needle visibility. For the i th image frame, which is acquired at elevation angle ϕ , the orthogonal needle line and the azimuth interval, Ω , are computed based on the camera-estimated needle axis. Moreover, the portion of the camera-estimated needle axis that overlaps with the i th image frame is identified. The intersection, if any, between this portion of the camera-estimated needle axis and the azimuth interval, Ω , represents a segment along the camera-estimated needle axis that is expected to enable high needle visibility within the i th frame. The segments along the camera-estimated needle axis that are expected to enable high needle visibility within the 2D image frames of the 3D volume form a section in the camera-estimated needle axis that is expected to achieve high needle visibility in the 3D ultrasound volume. In fact, this section is called the camera-estimated needle axis section with high needle visibility.

The computation of the camera-estimated needle axis section with high needle visibility based on the physical 2D image frames that are acquired by the 3D curvilinear probe to synthesize the 3D ultrasound volume requires accurate calculation of the elevation (sweep) spacing between the 2D frames. However, the number of 2D image frames that are employed to synthesize the ultrasound volume might be changed based on the configurations of ultrasound imaging system, which in turn alters the elevation spacing between the acquired 2D frames. An alternative approach is to compute the camera-estimated needle axis section with high needle visibility based on a set of virtual 2D image frames that are uniformly distributed within the ultrasound volume along the elevation direction. In particular, these virtual 2D image frames can be computed based on the known values of the elevation FOV, Φ , the aperture angle, Ψ , the rotation radius, a , and the radius of curvature, b , and the predetermined elevation spacing between the virtual frames. It is worth noting that the values of Φ , Ψ , a , and b are usually provided by the manufacturer. In this study, the camera-estimated needle axis section with high needle visibility is computed using virtual 2D image frames with uniform elevation spacing of 0.5° .

The camera-estimated needle axis section with high needle visibility is employed to define VOI_{Axis} that will be used to accurately localize the needle axis. In fact, VOI_{Axis} represents an approximate region around the camera-estimated needle axis section with high needle visibility that is hypothesized to include the needle. In this study, VOI_{Axis} is selected as a rectangular box with central axis located at the camera-estimated needle axis and length that matches the camera-estimated needle axis section with high needle visibility. The height and depth of VOI_{Axis} are set to 14 mm, which is equal to double the maximum error value computed for the camera-estimated needle axis as described in the Results section. The top face of VOI_{Axis} is oriented to be perpendicular to the “average” of the orthogonal needle lines of all 2D image frames that their azimuth intervals, Ω , overlap with the camera-estimated needle axis section with high needle visibility. This orientation ensures that the majority of the ultrasound beams that are perpendicular or nearly-perpendicular to the camera-estimated needle axis section with high needle visibility passes through the top face of VOI_{Axis} .

2.3.3. Analyzing VOI_{Axis} to localize the needle axis

To reduce the computational complexity, VOI_{Axis} is extracted from the ultrasound volume and all ultrasound-based computations to localize the needle axis are limited to VOI_{Axis} . The processing of VOI_{Axis} is carried out in two phases. In the first phase, VOI_{Axis} is analyzed to generate a 3D feature map using local phase analysis. In the second phase, the MF-RANSAC algorithm (Uherčík et al., 2010) is employed to accurately estimate the needle axis within VOI_{Axis} based on the 3D feature map. The estimated needle axis is mapped back to the 3D ultrasound volume.

Computing the 3D feature map

Our approach for extracting the 3D feature map is based on the phase congruency analysis introduced by Kovese (2003, 1999). In fact, the phase congruency, which quantifies points in the image at which the phase of the Fourier components are at their maximum, provides an intensity-invariant metric for detecting the edges (Kovese, 1999; Morrone et al., 1986; Kovese, 2003, 2000). The computation of the 2D phase congruency can be performed by employing even-symmetric and odd-symmetric log-Gabor filters that consider both the scale index, s , and the orientation index, o . Hence, the 2D phase congruency, $PC_o^{2D}(u, v)$, evaluated at orientation o can be written as (Kovese, 1999):

$$PC_o^{2D}(u, v) = \frac{\sum_s W_o(u, v) [A_{s,o}(u, v) \Delta\Gamma_{s,o}(u, v) - T_o]}{\sum_s A_{s,o}(u, v) + \eta}, \quad (1)$$

where $W_o(u, v)$ is the orientation-specific weighting function, $A_{s,o}(u, v)$ is the amplitude of the filter response at scale s and orientation o , $\Delta\Gamma_{s,o}(u, v)$ is the phase deviation at scale s and orientation o , T_o is the noise compensation term at orientation o , and η is a constant with small value to avoid zero denominator. A high value of $PC_o^{2D}(u, v)$ indicates a strong edge oriented along the direction o and a low value of $PC_o^{2D}(u, v)$ implies that there is no strong edge along this direction.

Since the majority of the ultrasound beams that are perpendicular or nearly-perpendicular to the camera-estimated needle axis section with high needle visibility passes through the top face of VOI_{Axis} , needle reflection of the ultrasound beams within VOI_{Axis} can be effectively detected by quantifying the edges that are parallel to the top face. In particular, we applied $PC_o^{2D}(u, v)$ to the 2D image planes that are extracted sequentially from VOI_{Axis} , such that the extracted 2D image planes are parallel to the front face of VOI_{Axis} . The computation of $PC_o^{2D}(u, v)$ is performed along the orientation orthogonal to the top face of VOI_{Axis} . The parameters of the 2D phase congruency analysis are set as described in (Kovese, 2000). The 3D feature map corresponds to the volume synthesized by processing VOI_{Axis} using the above-mentioned 2D phase congruency analysis. In fact, this 2D approach for computing the 3D feature map reduces the computational complexity by avoiding the computationally-intensive 3D phase congruency analysis.

Localizing the needle axis

The 3D feature map might include some false positive features that degrade the accuracy of estimating the needle axis. Therefore, the MF-RANSAC algorithm (Uherčík et al., 2010) is employed to accurately

localize the needle axis. To apply the MF-RANSAC algorithm, the 3D feature map is binarized using a thresholding procedure to generate a 3D binary volume. The thresholding is based on the fact that the strongest phase congruency features are expected to be located at the needle surface. The selection of the threshold is performed by examining eight threshold values that are the highest 50%, 40%, 30%, 20%, 15%, 10%, 5%, and 2% of the non-zero voxels in the 3D feature map. Our analysis indicated that setting the threshold value to the highest 10% of the non-zero voxels in the 3D feature map reduces the mean error of localizing the needle axis in all ultrasound volumes considered in this study. Moreover, our analysis showed that setting the threshold to values between the highest 5% and 15% of the non-zero voxels in the 3D feature does not lead to significant change in the accuracy of localizing the needle axis. Based on this analysis, a 3D binary volume is generated by setting the highest 10% of the non-zero voxels in the 3D feature map to one and the balance of the voxels to zero. To estimate the needle axis, the MF-RANSAC algorithm (Uherčík et al., 2010) is applied to the nonzero voxels in the 3D binary volume. In fact, the MF-RANSAC algorithm is configured to model the needle axis as a straight 3D line.

An illustrative example about the ultrasound-based analysis to localize the needle axis is provided in Fig. 5. In particular, Fig. 5(a) presents a 3D ultrasound volume acquired for a needle inserted in bovine muscle specimen. The figure shows the 2D plane that includes the needle, where the yellow arrow points to the high-visibility portion of the needle and the green arrow points to the needle tip. The approximate needle axis estimated using the camera is presented in Fig. 5(b). VOI_{Axis} is shown in Fig. 5(c) as part of the whole 3D ultrasound volume and in Fig. 5(d) as an extracted rectangular box. The 3D feature map computed using the 2D phase congruency analysis is presented in Fig. 5(e). Moreover, the needle axis obtained using the MF-RANSAC algorithm is shown in Fig. 5(f) as part of VOI_{Axis} . The estimated needle axis is mapped back to the 3D ultrasound volume as shown in Fig. 5(g).

2.4. Identifying the location of the needle tip

After the accurate localization of the needle axis, the position of the needle tip is identified by analyzing the voxels around the axis. Similar to the previous section, a VOI, denoted by VOI_{Tip} , is defined around the estimated needle axis. In particular, the central axis of VOI_{Tip} is located at the needle axis, its length extends across the entire 3D ultrasound volume, and its height and depth are set to 4 mm. These height and depth values are around three times the actual needle diameter, which limit the needle tip analysis to the local neighborhood around the needle axis. The orientation of VOI_{Tip} is set to match the orientation of VOI_{Axis} . Figures 6(a) and 6(b) show the VOI_{Tip} computed for the ultrasound volume in Fig. 5(a) overlaid on the ultrasound volume and as an extracted rectangular box, respectively.

The analysis of VOI_{Tip} is performed in two phases. In the first phase, VOI_{Tip} is processed to compute an intensity-invariant metric that can be processed to localize the tip. In particular, a 3D feature map is extracted from VOI_{Tip} based on the phase congruency analysis described in the previous section. Figure 6(c) shows the 3D feature map computed for VOI_{Tip} in Fig. 6(b). To enable robust estimation of the needle tip, the 3D feature map is projected on the needle axis using a moving window approach. The window

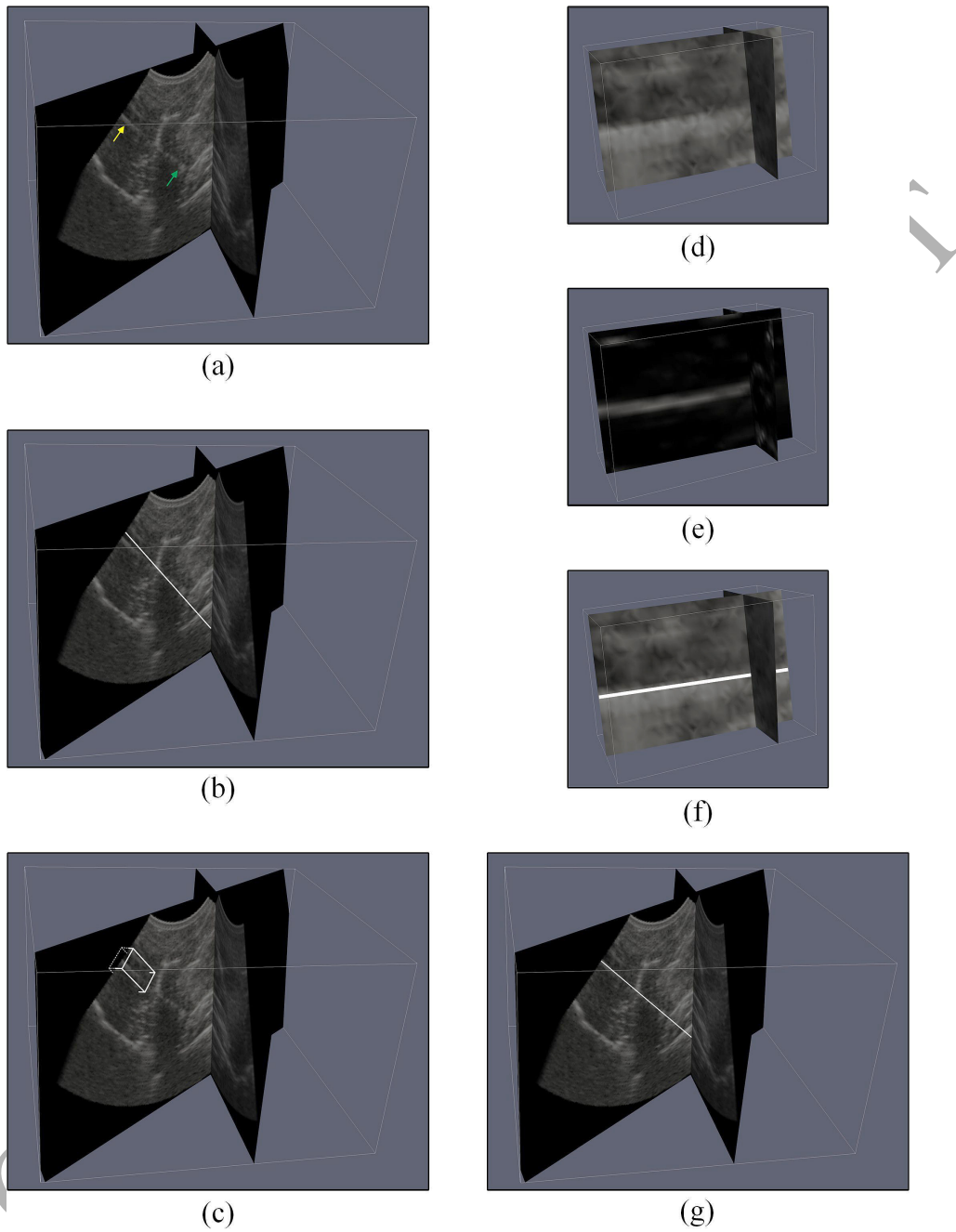


Figure 5: (a) A 3D ultrasound volume acquired for a needle inserted in bovine muscle specimen. The 2D plane that includes the needle is shown, where the yellow arrow points to the high-visibility portion of the needle and the green arrow points to the needle tip. (b) The camera-estimated needle axis. (c) and (d) VOI_{Axis} , which includes the high-visibility portion of the needle, is shown as part of the 3D ultrasound volume and as an extracted rectangular box, respectively. (e) The 3D feature map computed using phase congruency analysis. (f) and (g) The ultrasound-based estimation of the needle axis overlaid on VOI_{Axis} and on the entire 3D ultrasound volume, respectively.

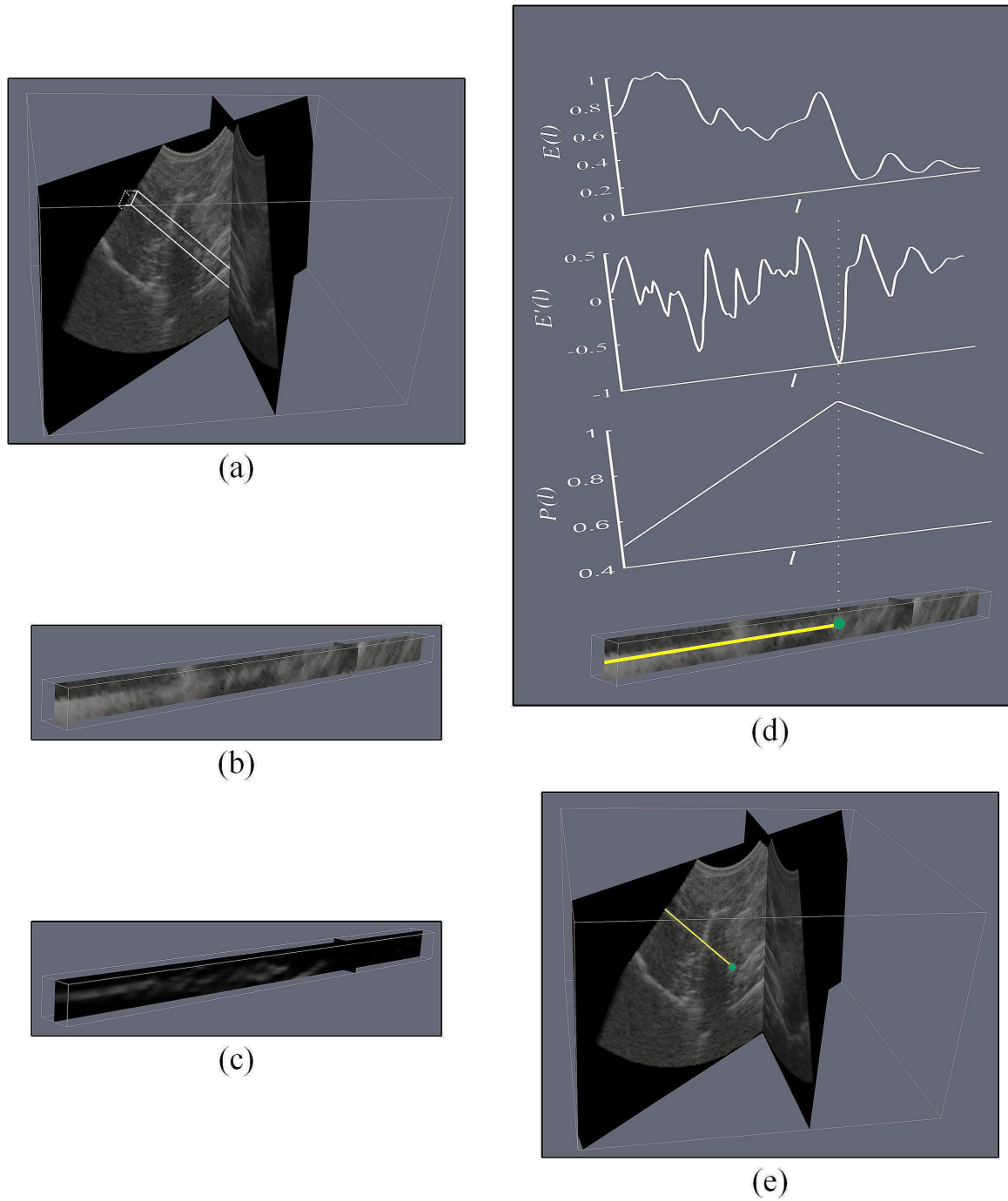


Figure 6: (a) and (b) VOI_{Tip} , which is used to localize the needle tip, is shown as part of the 3D ultrasound volume and as an extracted rectangular box, respectively. (c) The 3D feature map extracted from VOI_{Tip} using phase congruency analysis. (d) $E(l)$, $E'(l)$, and $P(l)$ computed to localize the needle tip. The localized needle axis and tip are overlaid on VOI_{Tip} , where the needle axis is shown as a yellow line and the needle tip is marked by a green circle. (e) The localized needle axis and tip are mapped back to the 3D ultrasound volume.

has a rectangular box structure with height, width, and length of 4 mm. The window is initially placed at
 460 the beginning of the needle axis (*i.e.* the entry point of the needle). The average value of the 3D feature
 map within the window is assigned to voxel located at the window's center. In the consecutive step, the
 window is shifted along the axis by one voxel and the average value of the feature map within the window
 is recomputed and assigned to the voxel at the center. The process of shifting the window and computing
 the average value of the 3D feature map is repeated until all voxels along the needle axis are covered by
 465 the moving window. Figure 6(d) shows the projected feature map, denoted by $E(l)$, where l represents the
 voxels along the needle axis. In this figure, $E(l)$ is normalized to values between 0 and 1.

In the second phase, $E(l)$ is processed to localize the needle tip. Similar to the 3D feature map, $E(l)$
 provides an intensity-invariant, orientation-specific metric to detect the edges that match the needle direction.
 Hence, when the axis of the needle is traversed from the entry point of the needle ($l = 0$) towards the needle
 tip, a sharp decay in $E(l)$ is expected at the needle tip. Such sharp decay leads to a large negative value
 in the spatial derivative of $E(l)$, *i.e.* $E'(l) = \frac{dE(l)}{dl}$. However, similar sharp decays in $E(l)$ might occur in
 other locations along the needle axis, which might limit the accuracy of localizing the needle tip. Another
 effective characteristic, which we also have used to identify the needle tip, is the fact that the majority of
 $E(l)$ values before the needle tip are expected to be high and the majority of $E(l)$ values after the tip are
 expected to be low. To quantify this characteristic, $E(l)$ is binarized using global thresholding in which the
 threshold is computed by applying Otsu's method (Otsu, 1979) on the non-zero points. In the binarized
 $E(l)$, which is denoted as $E_B(l)$, the white points from the entry point of the needle until the needle tip
 represent the correctly-detected needle voxels and the black points after the needle tip correspond to the
 correctly-identified non-needle voxels. Hence, the likelihood of a point, l , along the needle axis to be the true
 needle tip is proportional to $P(l)$:

$$P(l) = \frac{\sum_{i=0}^l E_B(i) + \sum_{i=l+1}^N (1 - E_B(i))}{N}, \quad (2)$$

where N is the total number of voxels along the needle axis. Figure 6(d) shows the normalized $E'(l)$ and
 $P(l)$ computed for the 3D feature map in Fig. 6(c).

To enable effective localization of the needle tip, both $E'(l)$ and $P(l)$ are analyzed. In particular, each
 470 peak in $P(l)$ represents a candidate point that might be the true needle tip. If multiple peaks exist in $P(l)$,
 then these peaks can be ranked based on the corresponding values of $E'(l)$. The peak of $P(l)$ with the
 highest negative value of $E'(l)$ is considered to be the needle tip. The plot of $P(l)$ presented in Fig. 6(d)
 shows a single peak, and hence the location of this peak is selected as the needle tip. It is worth noting that
 the highest negative value of $E'(l)$ in Fig. 6(d) is also located at the detected needle tip. At the bottom of
 475 Fig. 6(d), the estimated needle axis and tip are overlaid on the extracted VOI_{Tip} , where the needle axis is
 shown as a yellow line and the needle tip is marked by a green circle. The localized needle axis and tip are
 mapped back to the 3D ultrasound volume, as shown in Fig. 6(e).

2.5. Needle tracking procedure

Since needle insertion in the tissue is a dynamic process, the localization of the needle in an individual
 480 3D ultrasound volume is not sufficient in real-life clinical needle interventions. In fact, the application of
 our proposed needle localization method, which is described in subsections 2.2, 2.3, and 2.4, for tracking the
 needle in a sequence of 3D ultrasound volumes requires the needle to be visible for the camera during the
 acquisition of all ultrasound volumes. Such a requirement might impose some limitations on the use of the
 proposed method in real-life clinical interventions. To address this limitation, a needle tracking procedure
 485 is employed to limit the camera-visibility requirement to be mainly at the beginning of the 3D ultrasound
 imaging process.

The needle tracking process starts by detecting the needle axis and tip in the first volume of the ultrasound
 sequence using the camera- and ultrasound-based localization analyses described in subsections 2.2, 2.3, and
 2.4. For the remaining volumes, a tracking loop is used to estimate the needle location in the current, *i.e.*
 490 k th, volume by taking into consideration the needle location in the previous, *i.e.* $(k - 1)$ th, volume. The
 tracking loop is essentially based on the tracking procedure introduced in (Zhao et al., 2013).

The tracking loop employs a motion estimation algorithm to compute the insertion velocity of the needle
 tip. In this algorithm, the computation of the tip velocity is carried out by defining a small 3D region around
 the needle tip in the $(k - 1)$ th ultrasound volume and a larger region around the same location in the k th
 495 ultrasound volume. Both 3D regions are processed using a speckle tracking method (Trahey et al., 1988)
 to compute the tip velocity. The configurations of the 3D regions and the speckle tracking method match
 the tracking analysis described in (Zhao et al., 2013). The Kalman filter described in (Zhao et al., 2013) is
 adopted to track the needle in the k th ultrasound volume. In particular, the time update equations of the
 Kalman filter are employed to obtain an initial prediction of the needle axis in the k th ultrasound volume
 500 based on the needle location in the $(k - 1)$ th ultrasound volume and the tip velocity computed using the
 motion tracking algorithm. The initial prediction of the needle axis is used in the dynamic needle tracking
 situation as a substitution for the camera-based estimation of the needle axis. Hence, accurate tracking of
 the needle axis and tip in the k th ultrasound volume can be obtained by processing the initial prediction of
 the needle axis using the ultrasound-based analyses described in subsections 2.3 and 2.4. Specifically, the
 505 computation of VOI_{Axis} , which is described in subsection 2.3.2, is performed using the initial prediction of
 the needle axis instead of the camera-based estimation of the needle axis. Finally, the measurement update
 equations of the Kalman filter are used to refine the ultrasound-based estimations of the needle axis and tip
 computed for the k th ultrasound volume based on the needle tracking results of the $(k - 1)$ th volume.

Similar to (Zhao et al., 2013), an automatic error correction policy has been implemented to enable robust
 510 needle tracking. The policy is based on the assumption that needle insertion in the tissue usually follows a
 specific path and hence the locations of the needle in two consecutive ultrasound volumes are expected to be
 close. Therefore, if the difference between the needle axis in the k th ultrasound volume and the needle axis
 in the $(k - 1)$ th volume is greater than 3 mm, the tracking of the needle in the k th volume is considered to

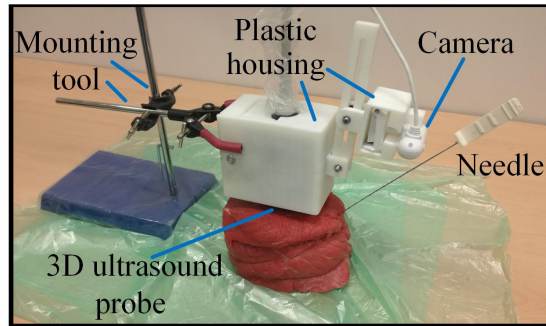


Figure 7: The experimental setup employed to image a needle inserted in a bovine muscle specimen.

be a failure. Hence, needle tracking in the k th ultrasound volume is re-initialized based on the camera-based
 515 estimation of the needle axis described in subsection 2.2.

3. Experiments

The performance of the proposed method is evaluated in terms of its ability to localize and track the
 needle. In particular, the accuracy of the camera-estimated needle axis, which is based on the study by
 Najafi et al. (2015), is quantified. Furthermore, the performance of our proposed method, which integrates the
 520 camera-based estimation of the needle axis with effective ultrasound-based analysis for localizing and tracking
 the needle, is evaluated and compared with the ROI-RK method (Zhao et al., 2013). These evaluations and
 comparisons are performed in both the static needle localization situation and the dynamic needle tracking
 situation using various *ex vivo* tissue types.

The proposed method, including the camera- and ultrasound-based analyses, and the ROI-RK method
 525 are implemented using MATLAB (The MathWorks Inc., Natick, MA, USA). Both methods are run on a
 computer workstation with Intel Xeon Processor (Intel Corporation, Santa Clara, CA, USA) operating at
 3.5 GHz and 16 GB memory.

3.1. Setup of the *ex vivo* animal experiments

Five bovine muscle specimens, five porcine muscle specimens, and five bovine liver specimens are used
 530 as imaging media. All tissue specimens were freshly excised and bought from a local butcher on the ex-
 periment day. The bovine muscle specimens, the porcine muscle specimens, and the bovine liver specimens
 provide imaging media with different ultrasound echogenicity characteristics. The needles employed in the
 experiments are standard biopsy needles with a diameter of 1.25 mm.

A mounting tool was used to hold the imaging apparatus, which includes the 3D ultrasound probe, the
 535 USB camera, and the plastic housing. For each tissue specimen, the needle was inserted manually to an
 insertion depth within the range of 40 to 90 mm. The needle insertion angles were between 30° and 60°
 with respect to the skin. Figure 7 shows the experimental setup. During the insertion of the needle in
 each tissue specimen, the USB camera was used to track the advancing needle. Moreover, the ultrasound

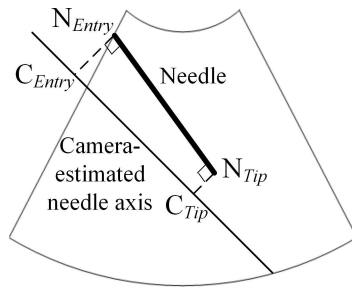


Figure 8: The computation of the needle axis error.

imaging system was used to acquire a sequence of ten 3D ultrasound volumes. The imaging depth of the
 540 ultrasound system was adjusted before starting the experiments to values between 50 and 90 mm, which
 enabled the acquisition of 3D ultrasound volumes with isotropic voxel sizes between 0.4 and 0.7 mm at frame
 rates between 1.6 and 1.8 volumes per seconds.

3.2. Performance analysis of the camera-based estimation of the needle axis

The performance of the camera-based estimation of the needle axis is quantified by estimating the needle
 545 axis in each individual volume of the acquired 3D ultrasound sequences and comparing the estimated axis
 with the axis of the matching ground truth needle. In fact, the ground truth needle was obtained using
 manual segmentation performed by a radiologist with more than 14 years of experience. In particular,
 the needle in each ultrasound volume was segmented manually for three times and the mean of the three
 segmentations is taken as the ground truth needle.

Two performance metrics are used to evaluate the camera-estimated needle axis, where these metrics
 550 are the axis error and the angle error. The axis error is based on the accuracy analyses reported in (Zhao
 et al., 2013) and (Zhao et al., 2017). Figure 8 illustrates the computation of the axis error. In this figure,
 the plane that includes the needle is shown, where N_{Entry} and N_{Tip} are the entry point and the tip of the
 ground truth needle, respectively, and C_{Entry} and C_{Tip} are the orthogonal projections of N_{Entry} and N_{Tip} ,
 555 respectively, on the camera-estimated needle axis. The axis error is evaluated by computing the Euclidean
 distance between N_{Entry} and C_{Entry} and the distance between N_{Tip} and C_{Tip} and taking the maximum of
 the two distances. The angle error is defined as the angle between the axis of the ground truth needle and
 the estimated needle axis.

For a given ultrasound volume, the camera-based estimation of the needle axis is considered as failure
 560 if the axis error is greater than a given tolerance distance. In this study, three failure rates, namely the
 failure rate with tolerance distance of 3 mm, the failure rate with tolerance distance of 5 mm, and the failure
 rate with tolerance distance of 10 mm, are computed to quantify the percentages of camera-based needle
 axis estimations that have axis error values greater than 3 mm, 5 mm, and 10 mm, respectively. Since

the camera-based analysis aims to provide approximate estimation of the needle axis, the mean \pm standard deviation of each one of the two evaluation metrics is calculated for the ultrasound volumes in which the axis error is less than 10 mm. In addition, the mean \pm standard deviation execution time needed to estimate the needle axis using the camera is reported.

3.3. Performance analysis of the static needle localization

The accuracy of localizing the needle in the static situation was evaluated by employing our proposed method and the ROI-RK method (Zhao et al., 2013) to localize the needle in each individual volume of the acquired 3D ultrasound sequences. In fact, needle localization in the static situation is performed by analyzing only the camera and ultrasound data of the volume under consideration without considering the localization results of the previous volume in the sequence. Hence, the tracking loops of our proposed method and the ROI-RK method (Zhao et al., 2013) are not employed. For each ultrasound volume, the process of localizing the needle using the two methods has been repeated for three times. Hence, the total number of evaluations is 450 (3 tissue types \times 5 specimens of each tissue type \times 10 ultrasound volumes acquired during needle insertion \times 3 evaluation trials performed for each volume).

The estimated coordinates of the needle axis and tip were compared with the matching ground truth needle coordinates. In fact, three metrics are employed to quantify the needle localization accuracy, where these metrics are the tip error, the axis error, and the angle error. The axis error and the angle error are calculated using the same procedure employed to evaluate the performance of the camera-based estimation of the needle axis, which was described in the previous subsection. The tip error is equal to the Euclidean distance between the ground truth needle tip and the estimated needle tip. In addition, three failure rates, namely the failure rate with tolerance distance of 3 mm, the failure rate with tolerance distance of 5 mm, and the failure rate with tolerance distance of 10 mm, are computed to quantify the percentages of the needle localization trials in which the axis error of the estimated needle is greater than 3 mm, 5 mm, and 10 mm, respectively. Since the task of localizing the needle aims to enable accurate estimation of the needle, the mean \pm standard deviation of each metric is calculated for the evaluation trials in which the axis error is less than 3 mm. Moreover, the mean \pm standard deviation execution time required to localize the needle is reported.

3.4. Performance analysis of the dynamic needle tracking

The accuracy of needle tracking is evaluated by employing our proposed method and the ROI-RK method (Zhao et al., 2013) to track the needle in each ultrasound volume sequence acquired during needle insertion. Therefore, all components of our proposed method and the ROI-RK method, including the needle tracking loop, are applied. For each ultrasound sequence, the two methods are run for three trials to track the needle. Hence, the total number of evaluation trials is 45 (3 tissue types \times 5 specimens of each tissue type \times 3 needle tracking trials performed for the ultrasound volume sequence acquired for each specimen).

The three performance metrics, which are described in the previous subsection, are used to compare the needle tracked in each ultrasound volume with the matching ground truth needle. Moreover, three failure rates, namely the failure rate with tolerance distance of 3 mm, the failure rate with tolerance distance of 5 mm, and the failure rate with tolerance distance of 10 mm, are computed. In fact, the failure rates with tolerance distances of 3 mm, 5 mm, and 10 mm are the percentages of the needle tracking trials in which the needle axis error of any volume in the ultrasound sequence exceeds 3, 5, and 10 mm, respectively. Since the task of tracking the needle is more challenging than the needle localization task, the mean \pm standard deviation of each evaluation metric is computed for the needle tracking trials in which the axis errors of all volumes in the sequence are less than 10 mm. Moreover, the mean \pm standard deviation execution time required to track the needle in a particular volume of the ultrasound sequence is computed.

3.5. Analyzing the effect of varying the number of needle marking points on the camera-based estimation of the needle axis

The camera-based estimation of the needle axis might be affected by clutter and lighting conditions, as well as other camera acquisition conditions, that can affect the capability of identifying the needle marking points in the camera images. Hence, an additional set of ten experiments are carried out to investigate the effect of varying the number of needle marking points in the camera images on the accuracy of the camera-based estimation of the needle axis. In these experiments, a standard biopsy needle with a diameter of 1.25 mm was inserted in a water bath. In each experiment, the ultrasound imaging system and the camera were used to acquire a 3D ultrasound volume and a camera image, respectively, for the needle. The camera images included six needle marking points, where these points were located outside the needle bath. Moreover, the imaging depth of the ultrasound system was set to 90 mm and the needle insertion depth and angle were within the range of 40 to 90 mm and 30° to 60° , respectively. It is worth noting that the experimental setup employed in the current study to investigate the effect of varying the needle marking points on the accuracy of the camera-based estimation of the needle axis, which is based on needles embedded in a water bath, is close to the setup employed by Najafi et al. (2015).

For each experiment, the camera-based estimation of the needle axis was repeated twelve times using 6, 5, 4, and 3 needle marking points, such that for each specific number of needle marking points the camera-based needle axis localization is repeated for three times. For the camera-based needle axis localization trials that were performed using a number of needle marking points lower than 6, the marking points employed to localize the needle axis in each trial were randomly selected from the 6 points that exist in the camera image. The accuracy of the camera-based localization of the needle axis was evaluated by computing the failure rates with tolerance distances of 3 mm, 5 mm, and 10 mm as well as the mean \pm standard deviation values of the needle axis error and needle angle error based on manual segmentations of the needle in the 3D ultrasound volumes.

Table 1: The performance results of the camera-based estimation of the needle axis computed for needles inserted in bovine muscle specimens, porcine muscle specimens, and bovine liver specimens. The failure rates with tolerance distances of 3 mm, 5 mm, and 10 mm are denoted by failure rate 3 mm, failure rate 5 mm, and failure rate 10 mm, respectively.

Tissue	Failure rate 3 mm	Failure rate 5 mm	Failure rate 10 mm	Axis error (mm)	Angle error (°)
Bovine muscle	88%	45%	0%	4.4 ± 1.2	3.2 ± 2.1
Porcine muscle	80%	51%	0%	4.5 ± 1.6	4.4 ± 2.8
Bovine liver	59%	45%	0%	4.0 ± 1.9	4.6 ± 2.2

4. Results

4.1. Results of the camera-based estimation of the needle axis

Table 1 presents the failure rates with tolerance distances of 3 mm, 5 mm, and 10 mm, which are denoted in the table by failure rate 3 mm, failure rate 5 mm, and failure rate 10 mm, respectively, that are computed for the camera-based axis estimations of the needles inserted in the three tissue types. These failure rates indicate that the majority of the axis errors computed for the camera-estimated needle axes are greater than 3 mm. Around half of the camera-estimated needle axes have error rates smaller than 5 mm. Furthermore, the camera-based analysis was able to estimate all needle axes with errors smaller than 10 mm. In fact, our analysis showed that all camera-estimated needle axes had axis error values smaller than 7 mm.

The mean \pm standard deviation values of the axis error and the angle error computed for the camera-estimated needle axes are also shown in Table 1. For the three tissue types, the mean values of the needle axis error are between 4.0 and 4.5 mm. Moreover, the mean values of the needle angle error are between 3.2° and 4.6°. The mean \pm standard deviation execution time required to estimate the needle axis in one ultrasound volume using the camera-based analysis is 0.08 ± 0.01 second.

4.2. Results of the static needle localization

Table 2 shows the failure rates with tolerance distances of 3 mm, 5 mm, and 10 mm, which are denoted in the table by failure rate 3 mm, failure rate 5 mm, and failure rate 10 mm, respectively, that are calculated for the needle localization estimations obtained using our proposed method and the ROI-RK method (Zhao et al., 2013). For the three tissue types, the axis errors of all needle localizations performed using our proposed method are lower than 3 mm. For the ROI-RK method, the axis errors of the needles inserted in bovine muscle, porcine muscle, and bovine liver specimens are 81.7%, 85.3%, and 78.7%, respectively, higher than 3 mm, 65.6%, 64.7%, and 59.3%, respectively, greater than 5 mm, and 42.2%, 45.3%, and 37.3%, respectively, greater than 10 mm. These results indicate that the proposed method, which combines the camera-based estimation of the needle axis along with effective ultrasound-based localization of the needle, can enable accurate localization of the needle axis.

Table 2: The performance results obtained by the proposed method and the ROI-RK method (Zhao et al., 2013) in the static situation when the two methods are used to localize needles inserted in bovine muscle specimens, porcine muscle specimens, and bovine liver specimens. The failure rates with tolerance distances of 3 mm, 5 mm, and 10 mm are denoted by failure rate 3 mm, failure rate 5 mm, and failure rate 10 mm, respectively.

Tissue	Method	Failure rate 3 mm	Failure rate 5 mm	Failure rate 10 mm	Tip error (mm)	Axis error (mm)	Angle error (°)
Bovine muscle	Proposed	0.0%	0.0%	0.0%	1.2 ± 0.8	0.6 ± 0.5	1.4 ± 0.9
	ROI-RK	81.7%	65.6%	42.2%	2.4 ± 1.5	1.8 ± 0.9	2.7 ± 1.6
Porcine muscle	Proposed	0.0%	0.0%	0.0%	1.0 ± 0.7	0.7 ± 0.5	1.6 ± 0.8
	ROI-RK	85.3%	64.7%	45.3%	3.2 ± 1.0	1.9 ± 0.7	3.3 ± 1.7
Bovine liver	Proposed	0.0%	0.0%	0.0%	0.9 ± 0.8	0.6 ± 0.6	1.7 ± 1.0
	ROI-RK	78.7%	59.3%	37.3%	2.6 ± 1.3	1.8 ± 0.8	4.3 ± 3.4

Table 2 also shows the mean \pm standard deviation values of the axis error, the angle error, and the tip error that are calculated for the proposed method and the ROI-RK method. The proposed method can localize the needle with mean axis errors between 0.6 and 0.7 mm, mean angle errors between 1.4° and 1.7° , and mean tip errors between 0.9 mm and 1.2 mm. In comparison, the ROI-RK method can localize the needle with mean axis errors between 1.8 and 1.9 mm, mean angle errors between 2.7° and 4.3° , and mean tip errors between 2.4 and 3.2 mm. It is worth noting that the error values of our proposed method are calculated based on all evaluation trials while the error values of the ROI-RK method are computed based on the evaluation trials in which its estimated needle has an axis error less than 3 mm.

The mean \pm standard deviation execution time required to estimate the needle in one ultrasound volume using the proposed method, including both the camera- and ultrasound-based analyses, is 0.32 ± 0.02 second. In comparison, the mean \pm standard deviation execution time needed to localize the needle using the ROI-RK method is 1.18 ± 0.04 second.

4.3. Results of the dynamic needle tracking

The values of the failure rate with tolerance distance of 3 mm obtained by employing our proposed method to track the needle insertions in the bovine muscle, porcine muscle, and bovine liver specimens are 6.7%, 0.0%, and 6.7%, respectively. Moreover, all values of the failure rate with tolerance distance of 5 mm and the failure rate with tolerance distance of 10 mm obtained by our proposed method for the three tissue types are equal to 0.0%. In comparison, the values of the failure rates obtained by the ROI-RK method for bovine muscle, porcine muscle, and bovine liver are 100%, 100%, and 100%, respectively, when the tolerance distance is 3 mm, 100%, 93.3%, and 93.3%, respectively, when the tolerance distance is 5 mm, and 60.0%, 66.7%, and 60.0%, respectively, when the tolerance distance is 10 mm. These results demonstrate the ability of the proposed method to effectively track the needle.

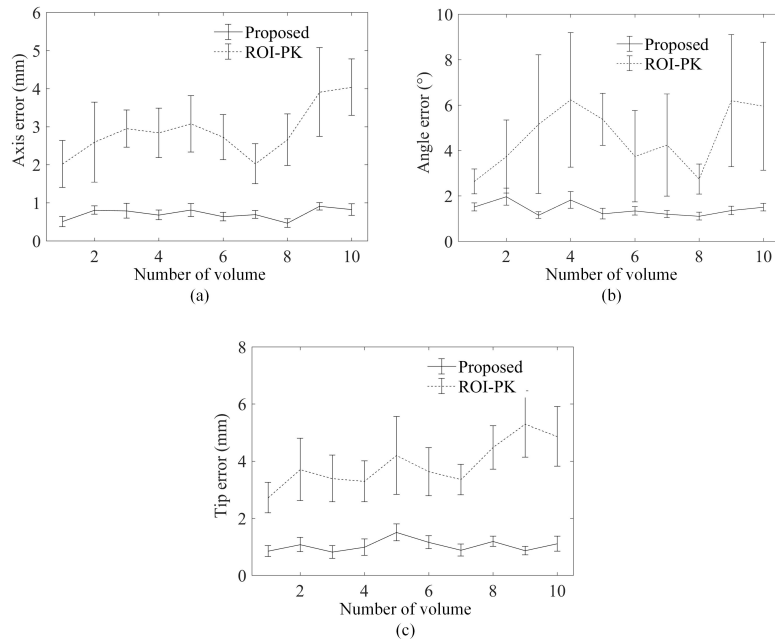


Figure 9: The mean \pm standard error values of the (a) axis error, (b) angle error, and (c) tip error obtained when the proposed method and the ROI-RK method (Zhao et al., 2013) are used to track the needles inserted in bovine muscle specimens.

The tracking accuracy results obtained for the needles inserted in bovine muscle, porcine muscle, and bovine liver specimens are shown in Figs. 9, 10, and 11, respectively, as a function of the number of the acquired ultrasound volume. The tracking error values of our proposed method are computed based on all evaluation trials. However, the error values of the ROI-RK method are obtained using 40.0%, 33.3%, and 40.0% of the needle tracking trials performed for the bovine muscle, porcine muscle, and bovine liver specimens, respectively, in which the axis errors of all volumes in the ultrasound sequence are less than 10 mm. For all tissue types, our proposed method tracked the needles with mean axis errors between 0.4 and 1.0 mm, mean angle errors between 1.1° and 2.0°, and mean tip errors between 0.8 and 1.7 mm. In comparison, needle tracking using the ROI-RK method achieved mean axis errors between 1.7 and 4.7 mm, mean angle errors between 2.6° and 7.3°, and mean tip errors between 2.1 and 7.2 mm. The tracking results of our proposed method indicate that increasing the volume number within the ultrasound sequence generally did not lead to large increase in the mean error values. However, the tracking results of the ROI-RK method indicate that increasing the volume number within the ultrasound sequence generally degrades the accuracy of needle tracking.

The mean \pm standard deviation execution time needed to track the needle using the proposed method is 0.19 ± 0.01 second per ultrasound volume. In comparison, the mean \pm standard deviation execution time required by the ROI-RK method to track the needle in one ultrasound volume is 0.20 ± 0.02 second. It is worth noting that 16% of the computations performed by the proposed method to track the needle in the acquired 3D ultrasound sequences include needle tracking re-initializations in which the needle is estimated

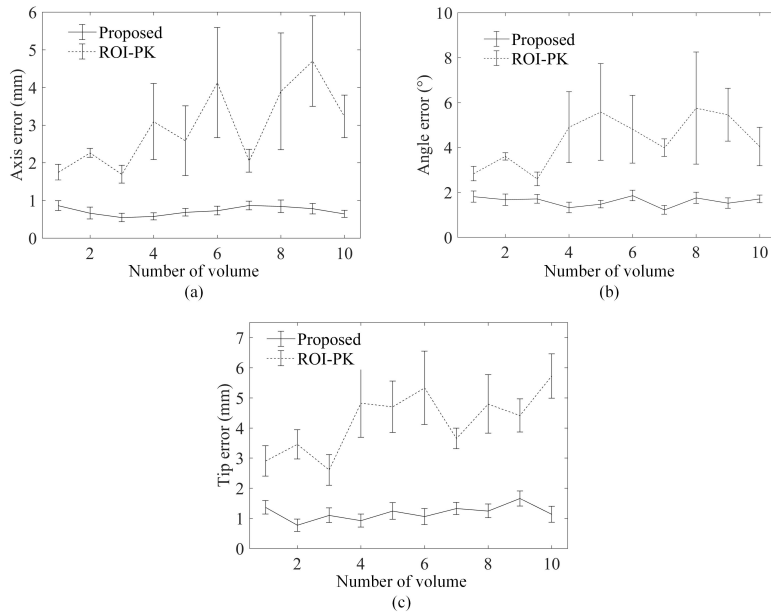


Figure 10: The mean \pm standard error values of the (a) axis error, (b) angle error, and (c) tip error obtained when the proposed method and the ROI-RK method (Zhao et al., 2013) are used to track the needles inserted in porcine muscle specimens.

in the ultrasound volume using the static needle localization procedure.

4.4. Quantitative analysis

700 Figures 12(a), 13(a), 14(a), and 15(a) present four ultrasound volumes acquired for needles inserted in *ex vivo* animal tissue specimens, where each volume is configured to show the plane that includes the needle. In particular, the needles in Figs. 12(a) and 13(a) are inserted in bovine muscle specimens. Moreover, the needles in Figs. 14(a) and 15(a) are inserted in porcine muscle specimen and bovine liver specimen, respectively. The four volumes have different ultrasound echogenicities and various needle visibility characteristics. The camera-based estimations of the needle axis obtained for the four ultrasound volumes are presented in Figs. 12(b), 13(b), 14(b), and 15(b). In fact, the camera-estimated needle axis of each volume is located in a plane that is slightly different from the plane that includes the needle. These camera-estimated needle axes demonstrate the capability of the camera-based analysis to obtain good approximation of the needle trajectory. The needle axis and tip that are localized using the ultrasound-based analysis are shown in Figs. 12(c), 13(c), 14(c), and 15(c). The localized needle axes and tips are close to the ground truth needles that are shown in Figs. 12(a), 13(a), 14(a), and 15(a). For comparison, the localization results obtained using the ROI-RK method (Zhao et al., 2013) are presented in Figs. 12(d), 13(d), 14(d), and 15(d).

4.5. Results of varying the number of needle marking point on the camera-based estimation of the needle axis

715 Table 3 shows the values of the failure rates with tolerance distances of 3 mm, 5 mm, and 10 mm, which are denoted in the table by failure rate 3 mm, failure rate 5 mm, and failure rate 10 mm, respectively, that

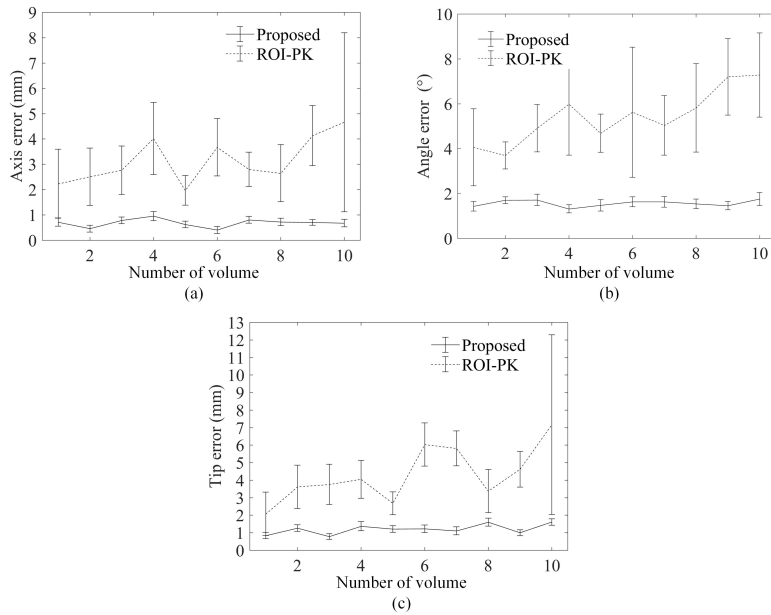


Figure 11: The mean \pm standard error values of the (a) axis error, (b) angle error, and (c) tip error obtained when the proposed method and the ROI-RK method (Zhao et al., 2013) are used to track the needles inserted in bovine liver specimens.

are computed for the camera-based estimation of the axes of the needles embedded in water bath using different numbers of needle marking points. As shown in the table, increasing the number of needle marking points from 3 to 4 reduces the values of both the failure rate with tolerance distance of 3 mm and the failure rate with tolerance distance of 5 mm by 10%. Moreover, increasing the number of needle marking points from 4 to 5 leads to reductions in the failure rates with tolerance distances of 3 mm and 5 mm by 6% and 13%, respectively. However, increasing the number of needle marking points from 5 to 6 improves the failure rates with tolerance distances of 3 mm and 5 mm by only 4% and 3%, respectively. For all examined values of needle marking points, the values of the failure rate with tolerance distance of 10 mm are equal to 0%, which indicates that all camera-estimated needle axes have axis error values that are smaller than 10 mm.

Table 3 also shows that increasing the number of needle marking points from 3 to 4 reduces the mean needle axis error and needle angle error values by 0.9 mm and 0.8° , respectively. Moreover, increasing the number of needle marking points from 4 to 5 reduces the mean needle axis error and mean needle angle error by 0.9 mm and 1.4° , respectively. However, increasing the needle marking points from 5 to 6 minimizes the mean needle axis error and mean needle angle error by only 0.2 mm and 0.3° , respectively. It is worth noting that the needle axis error values of all camera-based needle axis estimations obtained using 5 and 6 needle marking points are lower than 7 mm. However, for the camera-based needle axis estimations that are performed using 3 and 4 needle marking points, the needle axis error values can exceed 7 mm, but they are lower than 10 mm.

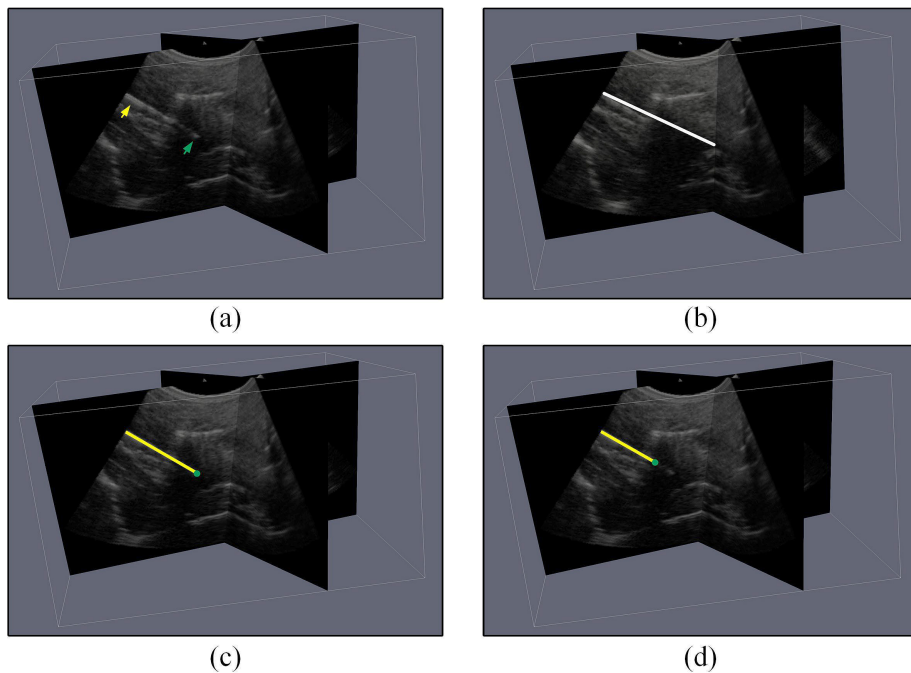


Figure 12: (a) A 3D ultrasound volume acquired for a needle inserted in bovine muscle specimen. The 2D plane that includes the needle is shown, where the yellow arrow points to the high-visibility portion of the needle and the green arrow points to the needle tip. (b) The camera-estimated needle axis. (c) The needle axis and tip estimated using the proposed method. (d) The needle axis and tip estimated using the ROI-RK method (Zhao et al., 2013). In (c) and (d), the needle axis is shown as a yellow line and the needle tip is marked by a green circle.

5. Discussion

735 The experimental results reported in the current study demonstrate the capability of our proposed method to enable accurate, reliable, and efficient localization and tracking of the needle using 3D curvilinear ultrasound volumes. In the static situation, the proposed method can localize the needle in the individual 3D ultrasound volumes with values of the failure rate with tolerance distance of 3 mm that are equal to 0% and maximum mean error values of 0.7 mm for the needle axis, 1.4° for the needle angle, and 1.2 mm for the needle tip. Moreover, the mean \pm standard deviation execution time required to localize the needle in
 740 the needle tip. Moreover, the mean \pm standard deviation execution time required to localize the needle in one ultrasound volume is 0.32 ± 0.02 second. In the dynamic situation, our proposed method can track the needle in a sequence of 3D ultrasound volumes with values of the failure rate with tolerance distance of 3 mm that are between 0% and 6.7% and values of the failure rate with tolerance distance of 5 mm that are equal to 0%. Moreover, the maximum mean error values computed for the dynamic needle tracking are equal to
 745 1.0 mm for the needle axis, 2.0° for the needle angle, and 1.7 mm for the needle tip. The mean \pm standard deviation execution time needed to track the needle is 0.19 ± 0.01 second per ultrasound volume. In the following, detailed discussion is provided for the methods and results reported in the previous sections.

The camera-based estimation of the needle axis has been demonstrated in the current study using a low-cost camera. The use of a low-cost camera introduces several challenges, including the limited field-

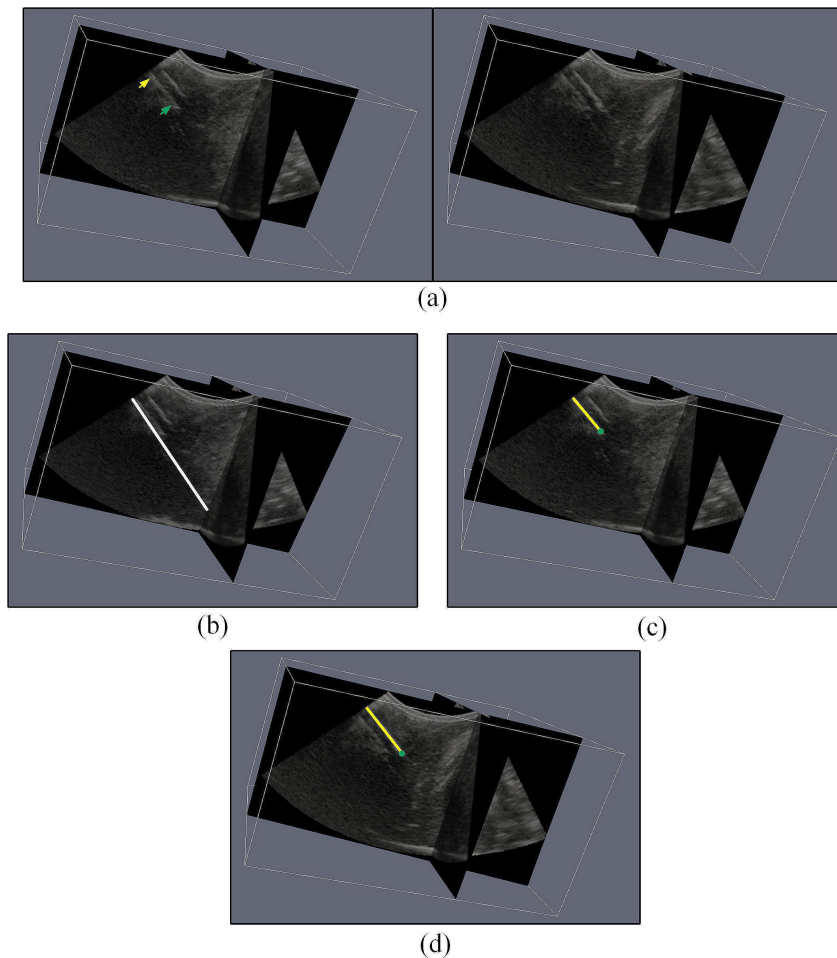


Figure 13: (a) A 3D ultrasound volume acquired for a needle inserted in bovine muscle specimen, in which a strong linear structure is located close to the needle. The left part of the figure shows a 2D plane in the ultrasound volume that includes the needle, where the yellow arrow points to the high-visibility portion of the needle and the green arrow points to the needle tip. Moreover, the right part of the figure shows a 2D plane in the ultrasound volume that includes the linear structure. (b) The camera-estimated needle axis. (c) The needle axis and tip estimated using the proposed method. (d) The needle axis and tip estimated using the ROI-RK method (Zhao et al., 2013). In (c) and (d), the needle axis is shown as a yellow line and the needle tip is marked by a green circle.

of-view and the low resolution. Despite these challenges, the results reported in Table 1 show that the low-cost camera was able to estimate the needle axis with mean axis errors on the order of 4 mm. Table 1 also indicates that the camera-based analysis, which is performed using a number of needle marking points greater than or equal to 5, can estimate the needle axis with maximum axis errors smaller than 7 mm. Hence, the width and height of VOI_{Axis} , which is defined around the camera-estimated needle axis to enable accurate ultrasound-based localization of the needle, are equal to two times the maximum limit of the camera axis error (*i.e.* 14 mm). In fact, the camera-based needle estimation accuracy results reported in Table 1 are lower than the accuracy results reported by Najafi et al. (2015), in which the needle position in a water bath was estimated by applying the same algorithm employed in the current study on images acquired by a high-performance camera. This difference in needle estimation accuracy can be attributed to the use of

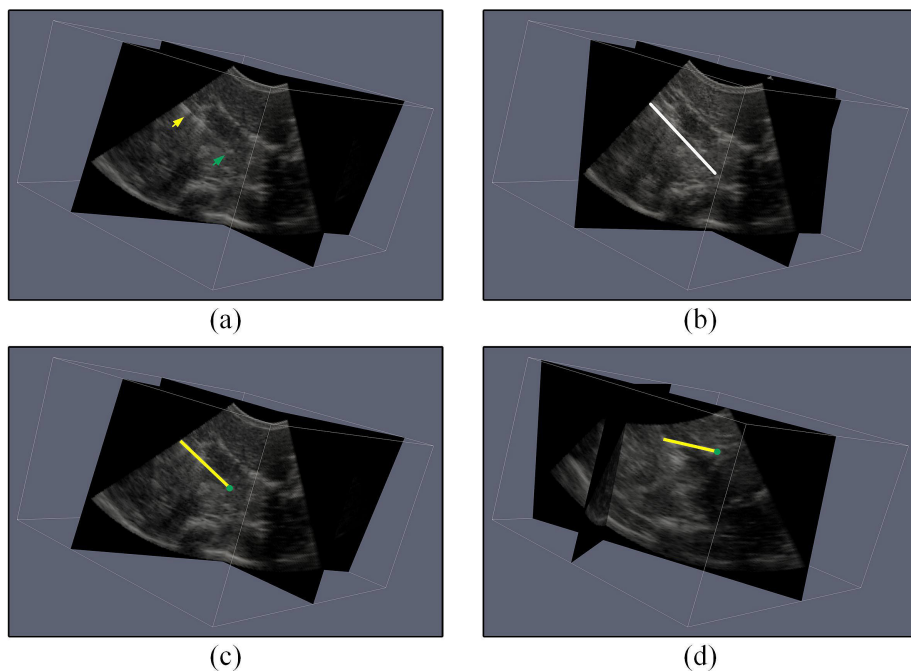


Figure 14: (a) A 3D ultrasound volume acquired for a needle inserted in porcine muscle specimen. The 2D plane that includes the needle is shown, where the yellow arrow points to the high-visibility portion of the needle and the green arrow points to the needle tip. (b) The camera-estimated needle axis. (c) The needle axis and tip estimated using the proposed method. (d) The needle axis and tip estimated using the ROI-RK method (Zhao et al., 2013). In (c) and (d), the needle axis is shown as a yellow line and the needle tip is marked by a green circle.

760 a low-cost camera, instead of a high-performance camera, to compute the needle axis position. A similar drop in the needle localization accuracy due to the use of low-cost cameras has been reported in (Chan et al., 2005), in which the mean camera-based needle localization accuracy was dropped from 3.1 mm using high-performance cameras to 6.5 mm using low-cost cameras. Hence, our proposed method may possibly be improved by using a camera with high resolution and wide field-of-view to estimate the needle axis.

765 Such an improvement may possibly lead to enhance the accuracy of the camera-based estimation of the needle axis using a lower number of needle marking points. Moreover, the performance of our proposed method may possibly be enhanced by using two cameras mounted on the ultrasound probe to estimate the needle axis. Such an enhancement is expected to enable the camera-based analysis to estimate the axis of a needle that does not have regular marking points. However, the use of two cameras or a single camera with

770 high specifications for estimating the needle axis is expected to increase the cost and the processing time requirements of our proposed method. In addition, the use of two cameras to estimate the needle axis might impose the need of maintaining direct line-of-sight between both cameras and the needle.

An important characteristic of our proposed method is the capability of the ultrasound-based analysis to refine the camera-based estimation of the needle axis, which has limited accuracy, to achieve accurate,

775 reliable, and efficient localization of the needle axis. In particular, the results presented in Table 2 show that

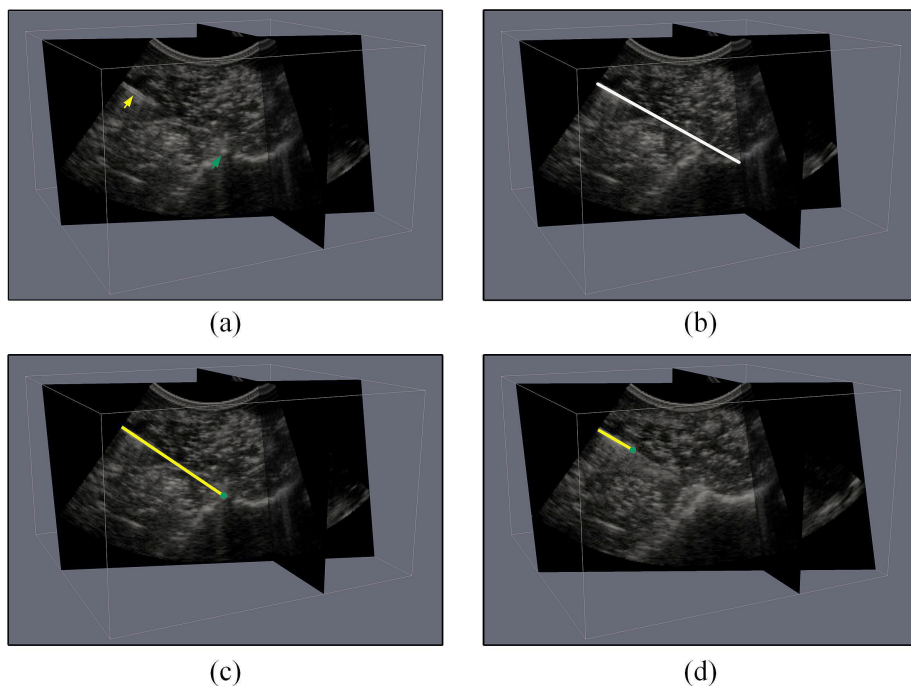


Figure 15: (a) A 3D ultrasound volume acquired for a needle inserted in bovine liver specimen. The 2D plane that includes the needle is shown, where the yellow arrow points to the high-visibility portion of the needle and the green arrow points to the needle tip. (b) The camera-estimated needle axis. (c) The needle axis and tip estimated using the proposed method. (d) The needle axis and tip estimated using the ROI-RK method (Zhao et al., 2013). In (c) and (d), the needle axis is shown as a yellow line and the needle tip is marked by a green circle.

the ultrasound-based analysis was able to localize the needle axis in all evaluation trials with axis error values smaller than 3 mm. Table 2 also shows that the ROI-RK method (Zhao et al., 2013) was able to obtain needle axis errors smaller than 3 mm, 5 mm, and 10 mm in only 14.7% to 21.3%, 34.4% to 40.7%, and 54.7% to 62.7%, respectively, of the evaluation trials performed for the three tissue types. In addition, the mean values of the needle axis error and angle error obtained by the proposed method for all evaluation trials are smaller than the matching mean error values achieved by the ROI-RK method for the evaluation trials in which the needle axis error is smaller than 3 mm. The capability of the proposed method to effectively localize the needle axis can be explained as follows. The ultrasound-based localization of the needle axis was performed using VOI_{Axis} , which is obtained by considering both the camera-based approximation of the needle axis and the imaging geometry of the 3D ultrasound probe. Hence, the computation of the needle axis, which is based on VOI_{Axis} , ensures that the needle axis localization process is performed based on a small region in the ultrasound volume that enables high needle visibility and limits the undesired interference of other irrelevant structures in the ultrasound volume. Moreover, limiting the needle axis localization analysis to VOI_{Axis} is crucial to minimize the computational complexity of our approach by avoiding the processing of other regions in the ultrasound volume that are not expected to provide high needle visibility. Furthermore, the local phase analysis of VOI_{Axis} , which is used to compute the 3D feature map, enables intensity-invariant, orientation-

Table 3: The performance results of the camera-based estimation of the needle axis computed for needles inserted in water bath using different numbers of needle marking points. The failure rates with tolerance distances of 3 mm, 5 mm, and 10 mm are denoted by failure rate 3 mm, failure rate 5 mm, and failure rate 10 mm, respectively.

Number of needle marking points	Failure rate 3 mm	Failure rate 5 mm	Failure rate 10 mm	Axis error (mm)	Angle error ($^{\circ}$)
3	93%	63%	0%	6.1 ± 2.2	6.4 ± 1.9
4	83%	53%	0%	5.2 ± 2.2	5.6 ± 1.6
5	77%	40%	0%	4.3 ± 1.6	4.2 ± 1.2
6	73%	37%	0%	4.1 ± 1.5	3.9 ± 0.7

specific detection of the edges that essentially match the direction of the camera-estimated needle axis. Due to these factors, the effects of speckle noise, ultrasound intensity variations, and needle-like structures that might exist in the ultrasound volume are minimized. It is worth noting that the intensity-based MF-RANSAC algorithm described in (Uherčík et al., 2010), which represents the main component of the static
795 needle localization phase of the ROI-RK method (Zhao et al., 2013), has been reported in (Uherčík, 2011) to have high failure rates in real ultrasound volumes with complex background.

Another advantage of the ultrasound-based needle localization analysis employed by our proposed method is the capability of reducing of the effect of the depth-dependent degrade in ultrasound lateral resolution,
800 which causes blurring and deformation artifacts. As described previously, the highest needle visibility in the ultrasound images and volumes acquired by curvilinear ultrasound probes is obtained when the ultrasound beams intercept perpendicularly or near perpendicularly with the needle (Daoud et al., 2015; Hacıhaliloglu et al., 2015). In fact, needle insertion in many real-life clinical interventions is performed at mid to steep insertion angles (Hacıhaliloglu et al., 2015). Hence, for curvilinear 2D transducers, the perpendicular or
805 near perpendicular interception between the needle and the ultrasound beams, which are transmitted by a transducer with convex shape, is expected to occur around a segment of the needle in which the distance between the needle and the transducer surface is reduced, *i.e.* at the closer needle segment to the transducer surface (Hacıhaliloglu et al., 2015). Similarly, the part of the needle that enables high needle visibility in a
810 3D ultrasound volume acquired by a motorized curvilinear ultrasound probe is also expected to be the closer needle part to the probe surface. This behavior can be seen in the 3D ultrasound volumes shown in Figs. 12, 13, 14, and 15. Due to this advantage, the effects of depth-dependent blurring and deformation artifacts is expected to be reduced inside VOI_{Axis} that surrounds the needle part with high visibility. Moreover, the ultrasound-based needle localization analysis performed by our proposed method, which employs intensity-invariant, orientation-specific, local phase analysis to identify the needle reflections inside VOI_{Axis} , are also
815 expected to reduce the effects of blurring and deformation.

The results presented in Table 2 also show that the proposed method was able to localize the needle tip in all evaluation trials with mean error values between 0.9 and 1.2 mm. These mean values of the tip

error are two to three times smaller than the matching values obtained by the ROI-RK method for the evaluation trials in which the needle axis error is smaller than 3 mm. The capability of the proposed method to accurately localize the needle tip is attributed to the probabilistic approach employed to analyze VOI_{Tip} that is generated around the localized needle axis. This probabilistic approach, which is based on intensity-invariant, orientation-specific local phase analysis, models the tip as a disconnection point along the needle axis in which the preceding points include edge features that match the needle direction and the succeeding points do not include such features.

The metrics employed to evaluate the performance of the dynamic needle tracking aim to quantify the capability to detect the needle in all volumes of a given ultrasound sequence, rather than test the ability to detect the needle in the individual ultrasound volumes as in the static needle localization situation. In particular, the failure rates with tolerance distances of 3 mm, 5 mm, and 10 mm that are computed in the dynamic needle tracking situation quantify the percentages of the needle tracking trials in which the needle axis error in any volume of the ultrasound sequence exceeds 3, 5, and 10 mm, respectively. In comparison, the computation of the three failure rate metrics in the static needle localization situation is performed based on the individual ultrasound volumes that are extracted from the 3D ultrasound sequences. Hence, the needle tracking performance analysis imposes higher requirements than the needle localization performance analysis. The needle tracking results obtained by the proposed method show that the values of the failure rate with tolerance distance of 3 mm obtained by employing our proposed method to track the needle insertions in the bovine muscle, porcine muscle, and bovine liver tissue specimens are 6.7%, 0.0%, and 6.7%, respectively. Moreover, all values of the failure rates with tolerance distances of 5 mm and 10 mm obtained by our proposed method for tracking the needle insertions in the three tissue types are equal to 0.0%. Hence, for each one of the 15 needle tracking trials that are performed for the porcine muscle tissue specimens, our proposed method succeeded to track the needle in all ten ultrasound volumes that compose the 3D ultrasound sequence with needle axis error values smaller than 3 mm. However, for the 30 needle tracking trials that are carried out for the bovine muscle and bovine liver tissue specimens, our proposed method succeeded to track the needle insertions in 28 needle tracking trials with needle axis error values smaller than 3 mm for all ultrasound volumes of the 3D ultrasound sequence. For each one of the two remaining tracking trials that are performed for the bovine muscle and bovine liver tissue specimens, our proposed method succeeded to track the needle with axis error values smaller than 3 mm for nine ultrasound volumes and needle axis error values between 3 and 5 mm for one of the ultrasound volumes that compose the 3D ultrasound sequence. The results presented in Figs. 9, 10, and 11 indicate that the mean values of the three performance metrics obtained by the proposed method for the three tissue types are relatively consistent throughout the needle tracking process. Moreover, the mean values of the three performance metrics achieved in the dynamic needle tracking situation are comparable with the performance metrics achieved by the proposed method in the static needle localization analysis. In comparison, for the vast majority of the needle tracking evaluation trials, the ROI-RK method failed to achieve needle axis errors

smaller than 5 mm for all volumes of the ultrasound sequence. For 33.3% to 40.0% of the needle tracking
 855 evaluation trials, the ROI-RK method was able to track the needle in all volumes of the ultrasound sequence
 with axis errors smaller than 10 mm. The results in Figs. 9, 10, and 11 indicate that the error metric values
 obtained by the ROI-RK method, which are computed for the tracking trials in which the axis errors of all
 volumes in the sequence are less than 10 mm, are substantially higher than the error metric values achieved
 by the proposed method. Furthermore, the results presented in Figs. 9, 10 and 11 suggest that the error
 860 of tracking the needle using the ROI-RK method generally exhibits an increasing trend as a function of the
 volume number.

As described previously, an important advantage of applying the needle tracking procedure of our pro-
 posed method is to limit the requirement of having direct line-of-sight between the camera and the nee-
 dle to the first ultrasound volume of the 3D ultrasound sequence and the incidents of needle tracking re-
 865 initialization. However, one constraint of applying the needle tracking procedure is the automatic error
 correction policy that assumes that the locations of the needle in two consecutive ultrasound volumes are
 expected to be close. In fact, this assumption implies that if the difference between of the tracked needle
 axis in the current ultrasound volume and the previous ultrasound volume exceeds 3 mm, then the dynamic
 tracking of the needle in the current volume is re-initialized by localizing the needle using the static needle
 870 localization procedure. This re-initialization process requires the physician to maintain direct line-of-sight
 between the camera and visible part of the needle located outside the body. Hence, in some clinical inter-
 ventions that might not satisfy this assumption, such as the situations in which the relative motion between
 the probe and the patient is high compared to the acquisition rate of the 3D ultrasound probe, the location
 of the needle should be determined by processing each individual 3D ultrasound volume separately using the
 875 static needle localization procedure, instead of applying the dynamic needle tracking procedure.

The execution time of the proposed method in the static needle localization situation is 3.7 times faster
 than the ROI-RK method. Moreover, the execution time of the proposed method in the dynamic needle
 tracking situation is comparable to the ROI-RK method. These execution time results can be explained
 as follows. In the static needle localization situation, the proposed method employed the camera-estimated
 880 needle axis to define VOI_{Axis} and all ultrasound-based analysis performed to refine the needle axis, including
 the phase congruency analysis and the MF-RANSAC algorithm, are limited to this VOI. Furthermore, the
 application of the MF-RANSAC algorithm, which represents a computationally-intensive component of the
 proposed method, is limited to the small set of edges that match the needle orientation. The refined needle
 axis is used to generate VOI_{Tip} and all needle tip computations are limited to this VOI. Hence, the proposed
 885 method was able to achieve a mean \pm standard deviation execution time of 0.32 ± 0.02 second. On the other
 hand, the needle axis estimation in the ROI-RK method involves the application of a 3D line filter on the
 whole ultrasound volume to obtain a 3D tubularness volume. The computationally-intensive MF-RANSAC
 algorithm is then applied on the entire tubularness volume to estimate the needle axis and tip. Hence, the
 mean \pm standard deviation execution time of the ROI-RK method to localize the needle is 1.18 ± 0.04

890 second. The execution time of our proposed method in the static situation is also lower than other previous
 methods that are introduced for localizing the needle in 3D ultrasound volumes, such as the method by
 Mwikirize et al. (2017) that has an execution time of around 3.5 second and the method by Pourtaherian
 et al. (2017) that has execution times between 2 and 4 minutes. In the dynamic needle tracking situation, the
 needle axis computations in the proposed method are limited to VOI_{Axis} that is estimated either using the
 895 Kalman filter, if there is no need for re-initialization, or using the camera-estimated needle axis, if there is a
 need for re-initialization. The estimation of the needle tip match the computations performed in the static
 needle localization situation. For the ROI-RK method, the computations performed to track the needle is
 limited to a small VOI that is estimated using the Kalman filter when there is no need for re-initialization.
 If there is a need to re-initialize, then the ROI-RK method applies the static needle localization algorithm.
 900 Therefore, the mean \pm standard deviation execution times of the proposed method and ROI-RK method in
 the dynamic needle tracking situation are equal to 0.19 ± 0.01 second and 0.20 ± 0.02 second, respectively.

One important factor that might affect the performance of our proposed method is the number of needle
 marking points employed to perform the camera-based estimation of the needle axis. In fact, the results
 reported in Table 3 indicate that the use of a number of needle marking points that is lower than 5, *i.e.*
 905 3 or 4, decreases the accuracy of the camera-based needle axis estimation. However, the results reported
 in subsection 4.5 indicate that the error of estimating the needles axes using the camera-based analysis did
 not exceed 10 mm regardless of the number of needle marking points employed to carry out the analysis.
 Based on these results, if the camera-based needle axis estimation is performed using a number of needle
 marking points that is lower than 5, then the size of VOI_{Axis} can be increased to enable the ultrasound-
 910 based analysis to localize the needle axis within a larger region around the camera-estimated needle axis.
 The analysis performed in the current study did not consider the effect of bending the needle on the accuracy
 of the camera-based analysis. In fact, since the camera-based analysis assume that the needle has a perfect
 linear structure, the error of estimating the needle axis using the camera is expected to be higher when the
 needle is bended during the insertion process. The effect of bending the needle can be handled by increasing
 915 the height and width of VOI_{Axis} to enable the ultrasound-based analysis to search for the needle within a
 larger region around the camera-estimated needle axis.

The results reported in the current study suggest that the proposed method provides a promising approach
 for localizing and tracking the needle in ultrasound sequences acquired using 3D motorized curvilinear
 probes. The future directions include the extension of the proposed method to support needle localization
 920 and tracking in 3D ultrasound sequences acquired by other types of 3D ultrasound probes, such as 3D
 phased-array ultrasound probes. Moreover, we plan to evaluate the proposed method using 3D ultrasound
 volume sequences obtained during *in vivo* needle insertion procedures. In fact, clinical application of our
 proposed method requires refining the size, shape, and layout of the plastic housing that attaches the camera
 to the ultrasound probe and the use of a smaller camera to improve the usability of the imaging apparatus
 925 in real-life medical applications. The execution time of the proposed method can be reduced using parallel

computing platforms, such as graphics processing units.

6. Conclusion

Needle localization and tracking in ultrasound volume sequences acquired using 3D motorized curvilinear ultrasound probes is essential to improve the performance of many ultrasound-guided needle insertion procedures. This study introduces a method to improve needle localization and tracking using 3D motorized curvilinear ultrasound probes. The method employs a low-cost camera mounted on the ultrasound probe to obtain an initial estimate of the needle axis. This initial estimate is refined by generating a VOI around the camera-estimated needle axis and applying ultrasound-based analysis to accurately localize the needle axis. The ultrasound-based analysis include the extraction of a local phase congruency map and the application of the MF-RANSAC algorithm. The location of the needle tip is determined using a probabilistic approach that quantifies the phase congruency around the estimated needle axis. Furthermore, the proposed method supports dynamic needle tracking in a sequence of 3D ultrasound volumes by incorporating a Kalman filter and a motion estimation algorithm. This needle tracking approach enabled effective estimation of the needle axis and tip in all volumes of the tracked ultrasound sequence and restricted the need for the camera-based estimation of the needle axis to be mainly at the first volume of the sequence. The proposed method was employed to localize and track needles inserted in different *ex vivo* animal tissue specimens. Moreover, the performance of the proposed method was compared with the ROI-RK method described in (Zhao et al., 2013). The results reported in the current study suggest the feasibility of applying the proposed method to localize and track the needle in 3D ultrasound volume sequences.

7. Acknowledgements

This research is supported by the Scientific Research Support Fund (project number ICT/1/20/2016), Jordan and the Seed Grant Program (project number SIC 21/2015), German Jordanian University, Amman, Jordan. Dr. Adnan Zayadeen from the Royal Medical Services, Jordan is acknowledged for manually segmenting the needles in the 3D ultrasound volumes.

References

- Adebar, T. K., & Okamura, A. M. (2013). 3D segmentation of curved needles using Doppler ultrasound and vibration. In *Proc. International Conference on Information Processing in Computer-Assisted Interventions* (pp. 61–70).
- Barva, M., Kybic, J., & Mari, J.-M. (2004). Radial radon transform dedicated to micro-object localization from radio frequency ultrasound signal. In *Proc. IEEE Ultrasonics Symposium* (pp. 1836–1839).

- Barva, M., Uhercik, M., Mari, J.-M., Kybic, J., Duhamel, J.-R., Liebgott, H., Hlavac, V., & Cachard, C. (2008). Parallel integral projection transform for straight electrode localization in 3-D ultrasound images. *IEEE Transactions on Ultrasonics, Ferroelectrics, and Frequency Control*, *55*, 1559–1569.
- Beigi, P., Rohling, R., Salcudean, T., Lessoway, V. A., & Ng, G. C. (2015). Needle trajectory and tip
960 localization in real-time 3-D ultrasound using a moving stylus. *Ultrasound in Medicine & Biology*, *41*, 2057–2070.
- Beigi, P., Rohling, R., Salcudean, T., Lessoway, V. A., & Ng, G. C. (2017). Detection of an invisible needle in ultrasound using a probabilistic SVM and time-domain features. *Ultrasonics*, *78*, 18–22.
- Cai, L., Wang, X., Wang, Y., Guo, Y., Yu, J., & Wang, Y. (2015). Robust phase-based texture descriptor
965 for classification of breast ultrasound images. *Biomed Eng Online*, *14*, 26.
- Chan, C., Lam, F., & Rohling, R. (2005). A needle tracking device for ultrasound guided percutaneous procedures. *Ultrasound in Medicine & Biology*, *31*, 1469–1483.
- Daoud, M., Rohling, R., Salcudean, S., & Abolmaesumi, P. (2015). Needle detection in curvilinear ultrasound images based on the reflection pattern of circular ultrasound waves. *Medical Physics*, *42*, 6221–6233.
- 970 Daoud, M. I., Abolmaesumi, P., You, W., Salcudean, S. E., & Rohling, R. N. (2011). Signature-based algorithm for improved needle localization in ultrasound images: A feasibility study. In *Proc. 2011 IEEE International Ultrasonics Symposium* (pp. 1575–1578).
- Ding, M., Cardinal, H. N., & Fenster, A. (2003). Automatic needle segmentation in three-dimensional ultrasound images using two orthogonal two-dimensional image projections. *Medical Physics*, *30*, 222–
975 234.
- Fischler, M. A., & Bolles, R. C. (1981). Random sample consensus: a paradigm for model fitting with applications to image analysis and automated cartography. *Communications of the ACM*, *24*, 381–395.
- Fronheiser, M. P., Idriss, S. F., Wolf, P. D., & Smith, S. W. (2008). Vibrating interventional device detection using real-time 3-D color Doppler. *IEEE Transactions on Ultrasonics, Ferroelectrics, and Frequency
980 Control*, *55*, 1355–1362.
- Gao, H., Huang, Q., Xu, X., & Li, X. (2016). Wireless and sensorless 3D ultrasound imaging. *Neurocomputing*, *195*, 159–171.
- Gebhard, R. E., Eubanks, T. N., & Meeks, R. (2015). Three-dimensional ultrasound imaging. *Current Opinion in Anaesthesiology*, *28*, 583–587.
- 985 Hacihaliloglu, I., Abugharbieh, R., Hodgson, A., & Rohling, R. (2009). Bone surface localization in ultrasound using image phase-based features. *Ultrasound Med Biol.*, *35*, 1475–87.

- Hacihaliloglu, I., Abugharbieh, R., Hodgson, A., Rohling, R., & Guy, P. (2012). Automatic bone localization and fracture detection from volumetric ultrasound images using 3-D local phase features. *Ultrasound Med Biol.*, *38*, 128–44.
- 990 Hacihaliloglu, I., Beigi, P., Ng, G., Rohling, R., Salcudean, S., & Abolmaesumi, P. (2015). Projection-based phase features for localization of a needle tip in 2D curvilinear ultrasound. In *Proc. 18th International Conference Medical Image Computing and Computer-Assisted Intervention – MICCAI 2015* (pp. 347–354).
- Harris, E. J., Miller, N. R., Bamber, J. C., Evans, P. M., & Symonds-Taylor, J. R. (2007). Performance of
995 ultrasound based measurement of 3D displacement using a curvilinear probe for organ motion tracking. *Physics in Medicine & Biology*, *52*, 5683—5703.
- Heikkila, J., & Silven, O. (1997). A four-step camera calibration procedure with implicit image correction. In *Proc. IEEE Computer Society Conference on Computer Vision and Pattern Recognition* (pp. 1106–1112).
- 1000 Holm, H., & Skjoldbye, B. (1996). Interventional ultrasound. *Ultrasound in Medicine & Biology*, *22*, 773–789.
- Khosravi, S., Rohling, T., & Lawrence, P. (2007). One-step needle pose estimation for ultrasound guided biopsies. In *Proc. 29th Annual International Conference of the IEEE Engineering in Medicine and Biology Society* (pp. 3343–3346).
- Kovesi, P. (1999). Image features from phase congruency. *Videre: Journal of Computer Vision Research*, *1*,
1005 1–26.
- Kovesi, P. (2000). Phase congruency: a low-level image invariant. *Psychological Research*, *64*, 136–148.
- Kovesi, P. (2003). Phase congruency detects corners and edges. In *Proc. 18th International Conference Medical Image Computing and Computer-Assisted Intervention – MICCAI 2015* (pp. 309–318).
- Mari, J. M., & Cachard, C. (2007). Acquire real-time RF digital ultrasound data from a commercial scanner.
1010 *Electronic Journal Technical Acoustics*, *3*, 1–16.
- Morrone, M., Ross, J., Burr, D., & Owens, R. (1986). Mach bands are phase dependent. *Nature*, *324*, 250–253.
- Mung, J., Vignon, F., & Jain, A. (2011). A non-disruptive technology for robust 3D tool tracking for ultrasound-guided interventions. In *Proc. Medical Image Computing and Computer-Assisted Intervention*
1015 *tion* (pp. 153–160).
- Mwikirize, C., Noshier, J. L., & Hacihaliloglu, I. (2017). Local phase-based learning for needle detection and localization in 3D ultrasound. In *Computer Assisted and Robotic Endoscopy and Clinical Image-Based Procedures* (pp. 108–115).

- 1020 Najafi, M., Abolmaesumi, P., & Rohling, R. (2015). Single-camera closed-form real-time needle tracking for
ultrasound-guided needle insertion. *Ultrasound in Medicine & Biology*, *41*, 2663–2676.
- Najafi, M., & Rohling, R. (2011). Single camera closed-form real-time needle trajectory tracking for ultra-
sound. *Proc. SPIE*, *7964*, 79641F.
- 1025 Neshat, H. R., & Pateluchi, R. V. (2008). Real-time parametric curved needle segmentation in 3D ultra-
sound images. In *Proc. 2nd IEEE RAS & EMBS International Conference on Biomedical Robotics and
Biomechatronics* (pp. 670–675).
- Novotny, P. M., Cannon, J. W., & Howe, R. D. (2003). Tool localization in 3D ultrasound images. In *Proc.
6th International Conference Medical Image Computing and Computer-Assisted Intervention - MICCAI
2003* (pp. 969–970).
- 1030 Novotny, P. M., Stoll, J. A., Vasilyev, N. V., del Nido, P. J., Dupont, P. E., Zickler, T. E., & Howe, R. D.
(2007). GPU based real-time instrument tracking with three-dimensional ultrasound. *Medical Image
Analysis*, *11*, 458–464.
- Oppenheim, A., & Lim, J. (1981). The importance of phase in signals. *Proc. IEEE*, *69*, 529–541.
- Otsu, N. (1979). A threshold selection method from gray-level histograms. *IEEE Transactions on Systems,
Man, and Cybernetics*, *9*, 62–66.
- 1035 Pospisil, E. R., Rohling, R., Azar, R. Z., & Salcudean, S. E. (2010). 4-D x 3-D ultrasound: real-time scan
conversion, filtering, and display of displacement vectors with a motorized curvilinear transducer. *IEEE
Transactions on Ultrasonics, Ferroelectrics, and Frequency Control*, *57*, 2271–2271.
- Pourtaherian, A., Scholten, H. J., Kusters, L., Zinger, S., Mihajlovic, N., Kolen, A. F., Zuo, F., Ng, G. C.,
Korsten, H. H. M., & de With, P. H. (2017). Medical instrument detection in 3-dimensional ultrasound
1040 data volumes. *IEEE Transactions on Medical Imaging*, *36*, 1664–1675.
- Prager, R., Rohling, R., Gee, A., & Berman, L. (1998). Rapid calibration for 3-D freehand ultrasound.
Ultrasound in Medicine & Biology, *24*, 855–869.
- Qiu, W., Ding, M., & Yuchi, M. (2008). Needle segmentation using 3D quick randomized hough transform.
In *Proc. First International Conference on Intelligent Networks and Intelligent Systems* (pp. 449–452).
- 1045 Trahey, G. E., Hubbard, S. M., & von Ramm, O. T. (1988). Angle independent ultrasonic blood flow
detection by frame-to-frame correlation of B-mode images. *Ultrasonics*, *26*, 271–276.
- Tsui, B., Doyle, K., Chu, K., Pillay, J., & Dillane, D. (2009). Case series: ultrasound-guided supraclavicular
block using a curvilinear probe in 104 day-case hand surgery patients. *Canadian Journal of Anesthesia*,
56, 46–51.

- 1050 Uherčík, M. (2011). *Surgical Tools Localization in 3D Ultrasound Images*. Ph.D. thesis Institut National des Sciences Appliquées, France.
- Uherčík, M., Kybic, J., Liebgott, H., & Cachard, C. (2010). Model fitting using RANSAC for surgical tool localization in 3-D ultrasound images. *IEEE Transactions on Biomedical Engineering*, *57*, 1907–1916.
- Wisniewski, S. J., Smith, J., Patterson, D. G., Carmichael, S. W., & Pawlina, W. (2010). Ultrasound-guided
1055 versus nonguided tibiotalar joint and sinus tarsi injections: A cadaveric study. *PM&R*, *2*, 277–281.
- Zhao, Y., Cachard, C., & Liebgott, H. (2013). Automatic needle detection and tracking in 3D ultrasound using an ROI-based RANSAC and Kalman method. *Ultrasonic Imaging*, *35*, 283–306.
- Zhao, Y., Shen, Y., Bernard, A., Cachard, C., & Liebgott, H. (2017). Evaluation and comparison of current biopsy needle localization and tracking methods using 3D ultrasound. *Ultrasonics*, *73*, 206–220.
- 1060 Zhou, H., Qiu, W., Ding, M., & Zhang, S. (2007). Automatic needle segmentation in 3D ultrasound images using 3D Hough transform. In *Proc. of SPIE Vol. 6789 - 5th International Symposium on Multispectral Image Processing and Pattern Recognition* (pp. 67890R 1–7).